IEEE Access
Multidisciplinary ⋮ Rapid Review ⋮ Open Access Journal

Received 18 August 2023, accepted 2 September 2023, date of publication 11 September 2023,
date of current version 20 September 2023.

Digital Object Identifier 10.1109/ACCESS.2023.3313981

RESEARCH ARTICLE

Kinematics of a Novel Serial-Parallel, Compliant, Three-Legged Robot

DAVID FELLER
Institute of Electrical Information Technology, Clausthal University of Technology, 38678 Clausthal-Zellerfeld, Germany
e-mail: david.feller@tu-clausthal.de

This work was supported by the Open Access Publishing Fund of the Clausthal University of Technology.

ABSTRACT In this article, the solution to the inverse and forward kinematics of a novel three-legged, serial-parallel, compliant robot are presented. The design of the robot aims to combine properties from serial and parallel architectures, thereby targeting an agile, yet precisely controllable robot that possibly allows both for dynamic locomotion and accurate manipulation tasks. The robot embodies the series connection of two parallel architectures, a planar and a spherical mechanism, realized in a highly dense mechanical assembly, allowing for lightweight, functionally redundant and compliant 4-DOF legs. A hybrid compliance behaviour is achieved, serving as a threshold between a stiff and compliant systemic state of the robot. Based on the mechanism design, the study involves the derivation of an alternative, yet complete solution for the inverse and forward kinematics of the spherical parallel manipulator (SPM). The approach utilizes spherical trigonometry and spatial vector geometry and yields a unique solution, while being both easy to implement and numerically efficient, thereby being applicable to real time implementations. Conceptually, a reduction of the mechanism assembly and working modes was directly integrated into the solution terms, drastically simplifying the expressions as they only represents the mechanically meaningful configuration relevant for actual physical systems. In addition to the active joint coordinates, the solution yields a unique set of all passively driven joints. The derived robot kinematics are furthermore verified through a 3D simulation model, showing the robot performing several motions. Thereby, the simulations portray the characteristics of the motor units by means of their corresponding phase profiles, revealing a balanced utilisation.

INDEX TERMS Forward kinematics, inverse kinematics, legged robot, mechanical design, serial-parallel mechanism, spherical parallel manipulator.

I. INTRODUCTION

Legged locomotion presents itself as a fascinating challenge in the field of legged robots. Over the years, a wide range of conceptually different mechanical designs was considered, modelled, simulated, and built in the vast literature of legged robots. Noticeably, many robots showed impressive results and are very capable to even traverse rough terrain, yet still strive to recreate the seemingly efficient and natural gait of biological beings.

With this work, we further explore the design of a novel legged robot, which is of rather atypical design due to its odd number of legs, if compared to examples from nature. However, the robot features the intricate combination of several mechanical ideas, which—as future work will investigate—might prove itself sufficient to allow for energy efficient legged locomotion. In this regard, as the robot design and a selection of its properties were discussed in our previous works [33], [34], [35], this article solely focusses on the complete inverse and forward kinematics of the robot. Since the robot consists of a large number of manifoldly connected mechanical parts in multiple interwoven closed loops, the kinematics of this robot are rather involved.

The associate editor coordinating the review of this manuscript and approving it for publication was Guilin Yang.

A. THE ROBOT CONCEPT

The five key concepts (I-V) [33] of the robot model—as depicted in Fig. 1—can be summarised as follows: Primarily, the three-legged design (I) marks the most

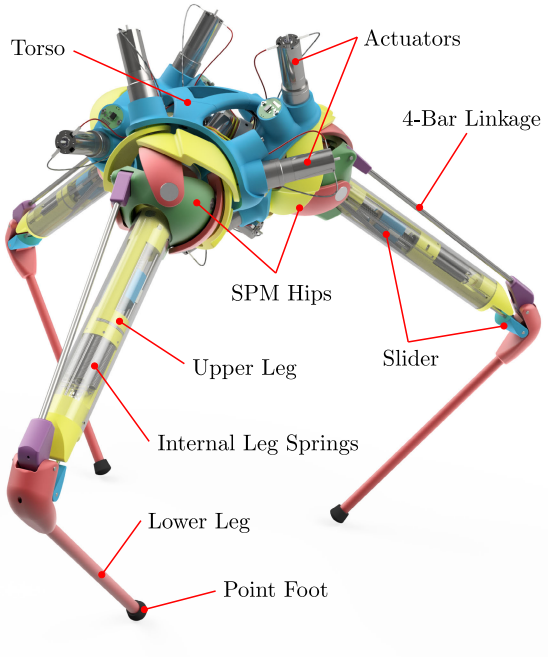

FIGURE 1. CAD model of the legged robot.

distinguishing factor in comparison to many other robots. A three-legged layout naturally requires dynamically balanced locomotion, considering only small contact surfaces per foot, yet does allow for statically stable object manipulation tasks in a tripodal posture. Crucially, minimizing the number of legs reduces the total weight of the robot, and may thus benefit agility during locomotion and allows for a better performance-weight-ratio. For reference, other three-legged designs were proposed in the literature [1], [10], [24], [26], [60], [62], [66], [68], [70]; however, those have largely different properties and target applications, as discussed in [33]. Similarly, the serial-parallel (II) actuation layout is an important property, which features a 3-degrees-of-freedom (DOF) motion of the hip joints via a spherical parallel mechanism, and a 1-DOF knee joint, connected in series. This hybrid design possibly allows for precise and strong hip motions, while still allowing for a suitable workspace due to the large range of motions provided by the knee joints. Furthermore, the hip joint features an internal load support structure (III) in a non-overconstrained design, which decouples external forces from motor torques. Thereby, due to the functional separation, a compact mechanism is achievable. Passive constraint forces and impacts from the locomotion cycle are captured in isolation by the internal universal joint, while only the required joint torques are transported through the hip parallel linkages. A similar approach was employed for the surgery robot in [14] that is based on a spherical parallel mechanism architecture and can support large load forces through an additional spherical joint placed in the manipulator centre. In a similar manner, our initial design of the robot in [34] utilized a passive spherical support joint as well. However, by replacing this spherical joint with an universal type mechanism that rotates with respect to the robot torso—equivalent to a serial RRR-joint—we can take advantage of the space within the hip centre, as it is required for the torque transmission from the actuators towards the knee joints. Furthermore, with the inclusion of a pre-stressed spring inside the upper leg, a planar 4-bar mechanism was realized in the leg plane, allowing for passive compliance (IV) of the leg, after passing a certain threshold. This yields a hybrid behaviour, and possibly allows the robot to perform object manipulation tasks in a statically determined and stiff configuration, while active locomotion transitions into a compliant, yet underactuated state. In addition, the overall design targets a dense mass concentration (V), which was achieved by placing all 12 actuators inside the robot torso, locating the robot centre of mass in the torso as well. Consequently, the robot legs may allow for fast and agile motions, as those embody only very small masses and inertias. Combining (I–V), the robot targets a behavioural similarity to the Spring-Loaded-Inverted-Pendulum (SLIP) template [11], [37], [77], which is studied in depth in the literature and may allow the application of corresponding control laws.

Consequently, as possible control laws implemented in the future work will require to express or reconstruct a body posture for either locomotion or precise object manipulation, the underlying kinematics based on the full body-joint structure must be explored.

B. RELATED WORK

Multiple aspects of the robot presented in this article were investigated in our previous works; however, the mechanical design of the robot was improved iteratively with each study, with the CAD model in Fig. 1 depicting the current version.

Initially, in [34] we presented a conceptual design of the robot, showing that legged locomotion over flat terrain is a feasible task with the general topology, utilizing a rigid-body simulation and a joint space PID control scheme. In [35] we substantially reworked the overall design and built a real world prototype of one of its legs. This iteration of the robot introduced the serial-parallel layout, featured a passive leg compliance and a dense mass concentration inside the robot torso, allowing for lightweight and agile legs. Furthermore, the general linearity of the leg compliance mechanism was shown. Recently, in [33], we examined multiple properties of the robot, including performance, dexterity and workspace analyses, with a particular focus on the hip joint conditioning, closeness to optimum isotropic postures and the potential risk to overload the actuators. Table 1 summarizes general properties of the robot.

C. ARTICLE SCOPE

The focus of this article lies on the complete mathematical derivation of the solution to the inverse and the forward

TABLE 1. Properties of the robot, derived from CAD based calculations, practical measurements and previous works [33], [34], [35].

Parameter	Value
Total mass of the robot	3130 g
Total mass of all 12 actuators	1290 g
Mass ratio Actuators–Robot	$1290/3130 \approx 0.412$
Mass ratio Skeleton–Robot	$(3130-1290)/3130 \approx 0.588$
Mass ratio Skeleton–Actuators	$(3130-1290)/1290 \approx 1.426$
Total number of actuated DOFs	12
Total number of compliant DOFs	3
Total number of bodies (assemblies)	55
Total number of joints	69
Total number of sensors devices	21
Hip: Maxon [47] DC-motor	DCX19S-GB-KL-18V
Hip: Maxon [47] gear head	GPX22-C-150:1
Hip: Mass of single DC-motor unit	115 g
Hip: Max. continuous motor torque	1.6 Nm
Hip: Sensor devices	12 units of RLS [69] RMB20
Knee: Maxon DC-motor	DCX19S-GB-KL-18V
Knee: Maxon gear head	GPX19-C-35:1
Knee: Mass of single DC-motor unit	85 g
Knee: Max. continuous motor torque	0.39 Nm
Knee: Sensor devices	3 units of RLS [69] RM08

kinematics of the robot model presented. These solutions were already implicitly used in the previous works in order to realize the according robot motions. To elaborate, the inverse kinematics yields the solution to all joint coordinates based on a given spatial position and orientation of the robot end-effectors. In this case, the location and rotation of the robot torso and of the feet points are given, which means that the inverse kinematics delivers the actuator angles for the corresponding robot posture. Likewise, the forward kinematics yield the current robot posture, based on the measured angles of the robot actuator joint axes.

Noticeably, a key part of the robot is the spherical parallel manipulator (SPM) utilized for the hip joints. Hence, in this article, the inverse kinematics specific to the general SPM are solved by the application of spherical trigonometry. In addition, the approach delivers the angular position of all active and passive joints inside the mechanism. Similarly, the SPM forward kinematics rely on spatial vector geometry. Both approaches differ from the usually utilized solutions from the literature. The implications and the comparison of these rather different approaches to the existing methods thus are important aspects, e.g. regarding numerical accuracy, complexity and execution speed; however, these analyses—more centric to the algorithms themselves—cannot be portrayed regarding the scope of this article. Still, multiple aspects made the usage of the geometric approaches beneficial for this specific application, as discussed in the following.

D. DISTINCTION TO OTHER METHODS

Despite there exist well known solutions to the kinematics of the SPM, the solution to this type of manipulator presented in this proposal is visually expressive and easy to implement in controller hardware. Both solutions to the inverse and the forward kinematics presented in the literature yield eight possible configurations of the manipulator; yet in practise, calculating the full set of solutions may not be required. In this regard—due to the geometric approach utilized in this article—the solution presented is unique, therefore it returns just one set of values, clearly defining the angular position for each axis in the case of the inverse kinematics problem. Correspondingly, a unique orientation of the tool platform is delivered in the forward kinematics case. Conceptually, the utilization of the geometric approach predetermines the physical configuration of the manipulator, and reduces the set of possible solutions, which corresponds to only one assembly mode for the forward solution and one working mode for the inverse solution. Consequently, the approach is practically motivated, as it considers only the actual mechanical structure of the manipulator, and may be considered as a special case that can be deduced from the more general literature methods. Since the produced solutions are simple expressions and display only first order root finding problems, the numerical requirements may be similar or possibly less demanding than the existing approaches.

1) INVERSE KINEMATICS

For reference, the often referred solution for the inverse kinematics in the literature was proposed in [38] and [44] with an algebraic approach. This approach was used for various applications, as e.g. in [74]. Alternatively, in [51] a solution based on spherical analytical theory was proposed. Recently, a solution based on projective angles was shown in [59]. In [61] a different geometric approach was shown specifically for the optimal SPM. In addition, related and similar solutions to the aforementioned methods were applied in [16], [27], [67], and [80].

Considering the geometrical approach—despite partial works were made in [48] and [49]—to the best of our knowledge, there has not been published a completely formulated solution for the general SPM, which is applicable to an arbitrary shape and is based on spherical trigonometry. This furthermore includes the representation of all nine joint coordinates and the initial embedding of a specific manipulator working mode that corresponds to the physically intended configuration of the mechanical system. However, the general application of spherical trigonometry for spherical mechanisms is a natural approach, as it was shown e.g. in [63]. Regarding other related spherically shaped robot mechanisms, spherical trigonometry was performed e.g. in [29] for the inverse kinematics solution of a dextrous robotic hand. Similarly, spherical trigonometry was used for the inverse and forward kinematics analysis of an eye surgery robot with spherical architecture [65]. In addition, the application of spherical trigonometry for similar problems was shown in [22], [25], [30], [75], and [76].

2) FORWARD KINEMATICS

Similarly, several methods were proposed for the solution to the forward kinematics problem of the SPM, as e.g.

reviewed in [9]. In [41] a polynomial approach was shown, which yields the Euler angles of the orientation matrix. In [51] the joint angles along the linkage chains were incorporated, also resulting in a polynomial expression. Furthermore, in [7] a solution based on input-output-equations (I/O) was proposed, which expresses the problem by two closed loops, connected by the same linkage part. All the aforementioned approaches yield polynomials of eight order due to the utilisation of trigonometric tan-half-angle identities. Alternatively, an interval propagation method was derived in [15]. A direct algebraic solution was presented in [54]. A geometric formulation yielding results for the individual assembly modes was shown in [61] for the optimal SPM. Basically, the problem solution can also be found by numerically solving a system of nine equations, expressing the constraint conditions of the assembly, as e.g. shown in [6], [78], [80], and [23]. Other related methods were applied in [53], [4], [12], [27], and [80].

Contrarily, in this work we propose a method for the forward kinematics that relies on a first order root finding problem with a single unknown variable. This is possible based on the restriction to a known assembly mode and the application on the optimal structural shape of the SPM. In this regard, the method has the drawback that it does not return all solutions to the SPM orientation, yet this might not be required under practical conditions, which will not switch assembly modes and may require short calculation times suitable for high speed real time applications. A different formulation by means of a unique solution to the forward kinematics problem was shown in [56], which similarly assumes that the manipulator remains in its current assembly mode; thus, does not cross a singularity configuration. However, in contrast to [56] the solution in this article is based on simple vector expressions. In [19] the idea was proposed to start the numerical solution from the initial guess of the last known posture. Similarly, this pre-assumes the actual posture of the manipulator and leads to a faster convergence of the numerical solution; however, the basic equations utilized in the approach were still formulated in a lengthy expression to support all theoretically attainable postures. Similarly, in order to obtain a unique solution from the numeric solver, in [81] the assembly mode was pre-assumed by starting from a specific guess vector. In [71], [72], and [50] an extra sensor was employed, shortening the required execution time by incorporating the additional information of the manipulator posture into the polynomial equations. In this regard, in [84] it is shown how the employment of additional sensors can greatly simplify the general polynomial solution to a forward kinematics problem of a parallel mechanism. However, in this article, due to the geometric approach, the proposed method fundamentally allows the variation of just one parameter, expressing the confined rotation of the tool platform, which only yields a feasible posture under specific constraint conditions. In a related manner, in [5] a geometric method based on a circle-line intersection problem of general four bar linkages was proposed. Crucially, the method in this article relies on a mechanical contextualization of the SPM orientation. By this measure, the set of unknowns is embedded into a expression of constrained motion, as there exist mechanical couplings between all variables. Thus, actually solving the forward kinematics problem can be thought of performing a constrained 1-DOF motion of the manipulator tool platform with one of the linkages being mechanically cut, until the required error tolerance at the joint axis is met.

E. ARTICLE STRUCTURE

The rest of the article is organized as follows: Sec. II briefly describes the robot model, initially presented in our previous works [33], [34], [35] and derives the representation model for the kinematics analysis. Sec. III then presents the solution for the full inverse kinematics of the legged robot. This section is partitioned in three subsections III-A, III-B and III-C as a result of the separation into smaller sub-problems. Specifically, Sec. III-C presents the solution to the inverse kinematics of the spherical parallel manipulator including all active and passive joints based on spherical trigonometry, which might be considered as a rather general solution, valid for any robot including the general SPM. Correspondingly, Sec. IV covers the complete forward kinematics solution of the robot model, including the geometrical approach of the forward kinematics for the SPM. For completeness, Sec. V shows the robot performing motion sequences based on the implemented solutions for the inverse and forward robot kinematics. Finally, Sec. VI discusses results and Sec. VII draws a conclusion. Additional mathematical expressions and figures are located in the Appendix.

II. THE ROBOT DESIGN

Fig. 1 depicts the CAD model of the three-legged robot, mostly composed of lightweight 3D-printed parts. The robot consists of 55 rigid bodies connected by 69 joints in total. The complete topology of the robot is shown in Fig. 2, visualizing the internal connections between the robot parts.

The general mechanical layout of the robot legs can be considered as a series connection of a spherical parallel manipulator—transmitting torque from the torso to the upper leg through the hip joint—and a planar parallel manipulator—defining the leg structure—which drives the knee joint. The hip joint is a spherical 3-DOF system and each actuator with the axes $\hat{\boldsymbol{u}}_1$, $\hat{\boldsymbol{u}}_2$ and $\hat{\boldsymbol{u}}_3$ is located inside the robot torso by a dense spatial arrangement. In addition, the knee actuator with axis $\hat{\boldsymbol{u}}_4$ was placed inside the torso as well; however, this actuator is connected via a bendable homokinetic transmission axis to the actual knee mechanism, reaching from axis $\hat{\boldsymbol{u}}_4$ to axis $\hat{\boldsymbol{c}}_9$. Thus, the knee actuator is connected in series to the set of the three hip base actuators, despite the knee actuator is not part of the moving leg itself. Furthermore, a passive torque around axis $\hat{\boldsymbol{c}}_3$ is produced by an internal spring located inside the upper leg, which is—beside the knee actuator—the other input force of the leg parallel mechanism.

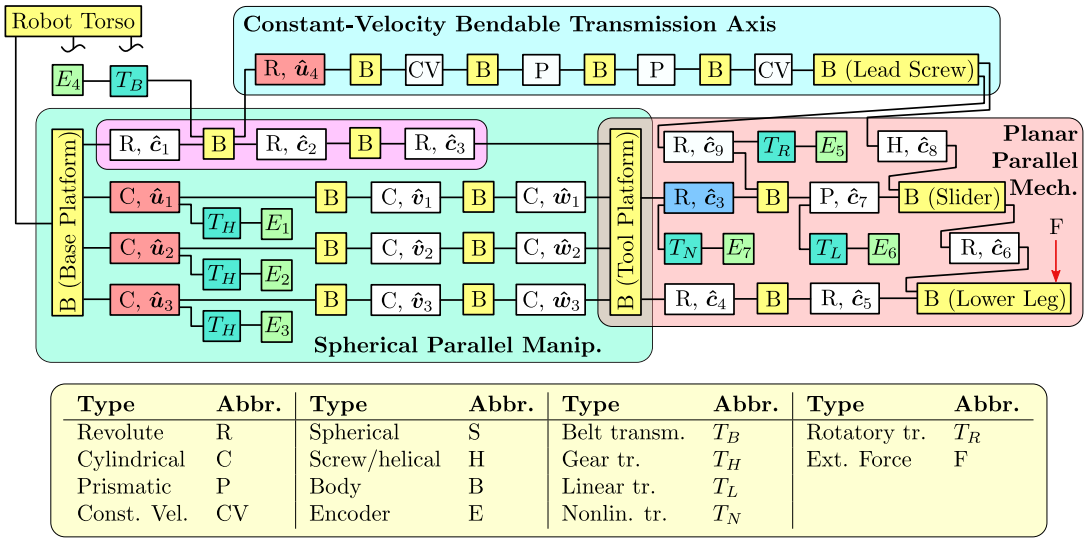

Type	Abbr.	Type	Abbr.	Type	Abbr.	Type	Abbr.
Revolute	R	Spherical	S	Belt transm.	T_B	Rotatory tr.	T_R
Cylindrical	C	Screw/helical	H	Gear tr.	T_H	Ext. Force	F
Prismatic	P	Body	B	Linear tr.	T_L		
Const. Vel.	CV	Encoder	E	Nonlin. tr.	T_N		

FIGURE 2. Topology of bodies and joints inside the robot model, based upon the diagram presented in [33]. Red joints are actively, blue joints passively actuated.

The connection between the application of the spring torque and the actual internal linear spring—composed of four pre-stressed springs in parallel arrangement—was realized by a high strength string, guided inside the upper leg over a system of multiple pulleys, finally connecting to the tool platform. This design was chosen to accommodate to the generally compact mechanical design. Applying the spring force through this string transmission results in a relative torque between upper leg and tool platform. The parallel leg system is composed of a planar four-bar mechanism—by the axes $\hat{\boldsymbol{c}}_3$, $\hat{\boldsymbol{c}}_4$, $\hat{\boldsymbol{c}}_5$ and $\hat{\boldsymbol{c}}_6$—that contains one side which can be length-adjusted by a slider mechanism via the prismatic axis $\hat{\boldsymbol{c}}_7$, driven by the knee actuator. The transmission of rotation from axis $\hat{\boldsymbol{c}}_9$ to translation on axis $\hat{\boldsymbol{c}}_7$ is realized by a screw joint on axis $\hat{\boldsymbol{c}}_8$.

The implemented leg compliance constitutes to a hybrid behaviour, which was shown in [35]. Thus, if external forces are below a certain threshold, the leg four-bar mechanism is effectively a 1-DOF manipulator based solely on the knee actuator. However, if external forces exceed the internal spring forces, the four-bar linkage deforms due to the angle between upper leg and tool platform on axis $\hat{\boldsymbol{c}}_3$ decreasing, resulting in a 2-DOF system. Thus, expressed by the spring slot angle φ_s, $\hat{\boldsymbol{c}}_3$ is allowing for a relative DOF between upper leg and tool platform. Consequently, in the relaxed posture of the leg, without external forces, the internal spring pulls the upper leg against the lower boundary of the slot that is carved into the tool platform.

Importantly, the axes $\hat{\boldsymbol{c}}_1$, $\hat{\boldsymbol{c}}_2$ and $\hat{\boldsymbol{c}}_3$ resemble a rotatable universal joint like support structure that allows spherical motion of the hip joint. Noticeably, axis $\hat{\boldsymbol{c}}_3$ is shared between both the universal joint and the spring DOF. Consequently, this RRR centre joint captures all forces introduced into the leg and allows the integration of an outer non-overconstrained 3-CCC parallel structure, transmitting the hip motor torque over the cylindrical axes $\hat{\boldsymbol{u}}_{1-3}$, $\hat{\boldsymbol{v}}_{1-3}$ and $\hat{\boldsymbol{w}}_{1-3}$.

To be able to fully reconstruct the robot posture, 21 joint sensors were included into the robot model. The absolute angular position of the base actuators are measured by the encoders E_{1-3}, connecting the measurement axes over T_H via helical gears of ratio 1.3, located inside the base platforms. The motion of the proximal universal joint structure around axis $\hat{\boldsymbol{c}}_1$ is measured over a miniature belt transmission T_B of ratio 23.5/7 by sensor E_4, which is actually partially redundant to the sensor data of E_{1-3}. In future work, this may allow for an improvement of the forward kinematics accuracy in the case that the hip joint moves closer towards a singular posture.

The slider position, controlling the knee angle, is captured by two sensors in tandem, E_5 and E_6. Sensor E_6 is an analogue linear potentiometer connecting with ratio 1 over T_L, and sensor E_5 is a single-turn, absolute high resolution contact-less encoder, directly connecting over T_R with ratio 1 to the lead screw axis. The implementation of two sensors stems from the requirement for absolute position information, which can only be assembled via the combination of E_5 and E_6. While E_5 is delivering the fine and absolute rotation of the lead screw, yet only as relative information, E_6 gives the broad, yet absolute slider position.

The compliant compression of the leg is observed with a linear potentiometer E_7, following the motion of the internal spring string, which yields a non-linear relationship T_N to the rotation axis $\hat{\boldsymbol{c}}_3$.

Currently, the robot does not include a battery or electronics; thus, it is dependent on a wired connection to both its power supply and its controller hardware. A complete real world prototype of this iteration is currently build in our laboratory.

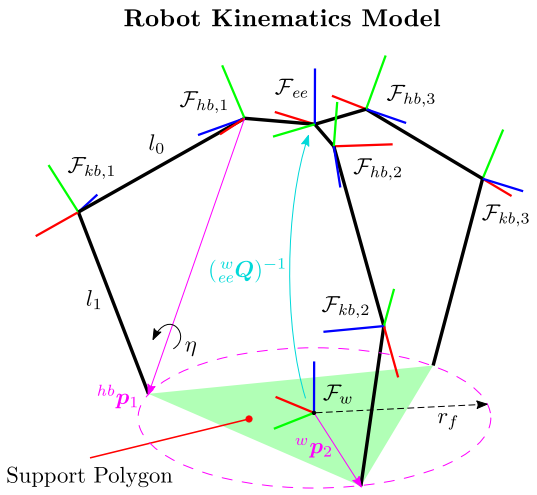

FIGURE 3. Simplified kinematics representation of the robot model, occluding the complexity of the internal mechanism.

A. NOTATION

Naturally, the formulation of the inverse and forward kinematics requires a description of the relative spaces between elements.

In the following, every matrix denoted with $\boldsymbol{R} \in \mathbb{R}^{3\times3}$ is an orthogonal linear mapping matrix belonging to the group SO(3); thus, matrices $\boldsymbol{R}$ express rotations. Matrices named with $\boldsymbol{Q} \in \mathbb{R}^{4\times4}$ express affine transformations; thus, $\boldsymbol{Q}$ expresses rotations in addition to translation. In general, transformation matrices $\boldsymbol{R}$ and $\boldsymbol{Q}$ describe the relative location and orientation of the base and follower reference frame of joints or bodies. In this regard, the joint base (b) and follower (f) frames are statically attached to different bodies, respectively. Hence, a vector ${}^{a}\boldsymbol{x}$ expressed in frame $\mathcal{F}_a$ is mapped into frame $\mathcal{F}_b$ by ${}^{b}\boldsymbol{x} = {}^{b}_{a}\boldsymbol{Q} \cdot {}^{a}\boldsymbol{x}$, with ${}^{b}_{a}\boldsymbol{Q}$ describing the joint transformation. In this case, vector $\boldsymbol{x}$ is extended by homogeneous coordinates, without specifically stating the dimensional change. Otherwise, a spatial vector $\boldsymbol{x}$ is always considered to obey to $\boldsymbol{x} \in \mathbb{R}^3$. If not stated otherwise, every norm $\|\cdot\|$ refers to the standard euclidean norm $\|\cdot\|_2$. A vector with hat-notation $\hat{\boldsymbol{x}}$ indicates that its length resolves to $\|\hat{\boldsymbol{x}}\| = 1$. Vectors $\hat{\boldsymbol{e}}_x$, $\hat{\boldsymbol{e}}_y$, $\hat{\boldsymbol{e}}_z$ are always parallel to the respective axis in an orthogonal reference frame $\mathcal{F}$. In some instances, the abbreviations c and s are used to allow for a short notation of the cos and sin functions, respectively. Table 4 in the appendix depicts the symbols and abbreviations used throughout this article.

B. KINEMATIC REPRESENTATION OF THE ROBOT MODEL

Since the robot is a complex mechanical system comprising serial and parallel structures, a multi-layered approach was employed in this work. Therefore, a simplified replacement model of the robot was defined, as depicted in Fig 3. In the following, the inverse kinematics of this model and the solution to the underlying more complex systems are presented.

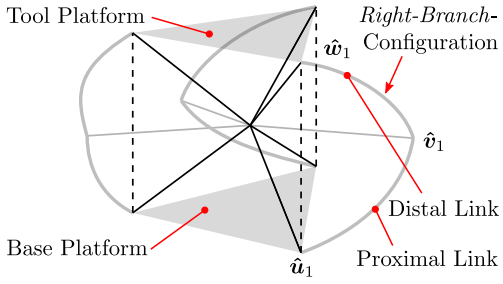

FIGURE 4. Naming convention for components of the hip manipulator employed in this work.

C. MATHEMATICAL SETUP OF THE SPM

The SPM is a 3-DOF orientation device and was examined in several works [3], [8], [13], [20], [38], [39], [40], [42], [43], [44], [45], [46], [51], [82] and was used in many applications [2], [18], [21], [27], [31], [36], [42], [46], [48], [49], [50], [55], [57], [58], [71], [72], [73], [74], [79], [83], [85]. Torque applied by the actuators in each of the three parallel linkages of the mechanism results in spherical rotation of the end-effector (EE) around the common centre point. Each part of the mechanism rotates around this centre; thus, each joint axis intersects in the centre. The linkages between base and end-effector are comprised of a proximal and distal link with the base, link and tool axes—called $\hat{\boldsymbol{u}}_j$, $\hat{\boldsymbol{v}}_j$ and $\hat{\boldsymbol{w}}_j$—connecting the parts in series. The individual parallel linkages of the manipulator are distinguished by the index $j \in 1, 2, 3$. In the following, the SPM end-effector is referred to as the tool platform. Fig. 4 depicts the naming convention for the SPM parts.

III. INVERSE KINEMATICS

As stated above, the solution to the inverse kinematics of the robot can be spilt into two separate problems. At first, the top-level kinematics of the robot are solved, considering the hip joint as a simple spherical joint and the knee as a revolute joint. This approximates the robot leg as a simple 2-link mechanism, effectively rendering the robot as a 3-SR system. Thus, for a known position and orientation of the robot torso and given target positions for each foot, the calculation of the generalized inverse kinematics yields a solution to the simplified kinematics substitute model (Sec. III-A). Based on the resulting transformation matrices expressing the relationship between joint and body frames, the calculation of the low-level kinematics is performed for the more complex underlying SPM and the leg mechanics (Sec. III-B–III-C). Finally, this yields the corresponding generalized actuator coordinates vector $\boldsymbol{\theta} \in \mathbb{R}^{12}$, due to the robot comprising 12 DC actuators for the actively driven joints.

A. GENERAL ROBOT INVERSE KINEMATICS

As a starting point, the matrix ${}^{w}_{ee}\boldsymbol{Q}$—defining the position and orientation of the robot torso in the world reference frame $\mathcal{F}_w$—is given. Furthermore, the target positions of each foot

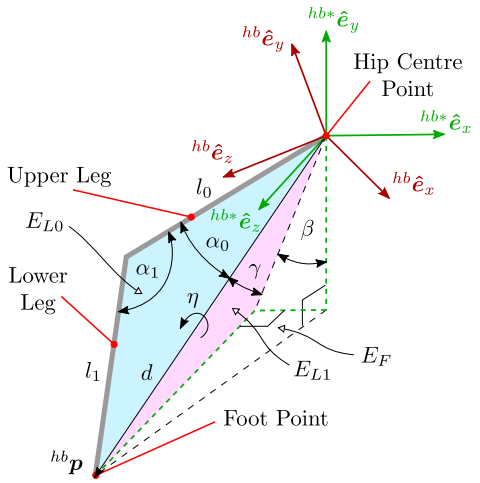

FIGURE 5. Simplified geometry for the general inverse kinematics. Variables l_0 and l_1 denote the lengths of upper and lower leg, respectively. It holds $E_{L0} \nparallel E_{L1}$ for the planes spanned inside the leg geometry if $\eta = 0$. Index i is omitted.

point are expressed with ${}^{w}\boldsymbol{p}_i$ for the legs $i = 1, 2, 3$ in the world reference frame. From the dimensions of the robot model, the static intermediate matrices ${}^{ee}_{hb}\boldsymbol{Q}_i$ are known, which describe the location of the SPM base platforms in the torso body. For readability, index i is omitted in the following.

Notably, the applicability of the inverse kinematics is directly related to the knowledge of the accurate position and orientation of the robot torso, expressed by the matrix ${}^{w}_{ee}\boldsymbol{Q}$. This matrix is a function of the external sensor information S depending on the employed hardware, thus:

$$ {}^{w}_{ee}\boldsymbol{Q} := f(S). \tag{1}$$

The value is fully known in the simulation as portrayed in this article; however, this aspect becomes relevant in the future real world implementation on an actual robot prototype, which relies on an estimate, accurate only to a certain degree in reality.

Based on the simplified robot kinematics model from Fig. 3 with SR type legs, the general top-level inverse kinematics of the robot are considered to be solved if the transformation matrices ${}^{hf}_{hb}\boldsymbol{R}$ for the spherical hip (S) joints and the internal angles α_1 expressing the revolute knee (R) joint orientation are determined. In this regard, the basic geometrical relationship for each leg can be observed in Fig. 5.

1) KNEE JOINT GENERAL KINEMATICS

At first, regarding the derivation of the knee joint angle α_1, the problem is projected into the base frames of the respective hip joints $\mathcal{F}_{hb}$. Therefore, a foot target position ${}^{w}\boldsymbol{p}$ with the component representation:

$$ {}^{w}\boldsymbol{p} = {}^{w}p_x\,{}^{w}\hat{\boldsymbol{e}}_x + {}^{w}p_y\,{}^{w}\hat{\boldsymbol{e}}_y + {}^{w}p_z\,{}^{w}\hat{\boldsymbol{e}}_z \tag{2}$$

is projected into the hip joint base frame by:

$$ {}^{hb}\boldsymbol{p} = {}^{hb}_{w}\boldsymbol{Q} \cdot {}^{w}\boldsymbol{p}, \tag{3}$$

with the transformation matrix:

$$ {}^{hb}_{w}\boldsymbol{Q} = \left({}^{w}_{ee}\boldsymbol{Q} \cdot {}^{ee}_{hb}\boldsymbol{Q}\right)^{-1}. \tag{4}$$

The distance between the hip and feet positions is determined by the norm $d = \|{}^{hb}\boldsymbol{p}\|$, which then allows for the calculation of the angles inside the leg planes E_{L0} and E_{L1}. However, as the actual leg is comprised of a complex mechanism, the length l_0 of the upper leg as depicted in Fig. 5 is not a constant parameter. Consequently, this value is the result of the nonlinear mapping function:

$$ l_0 := f_L(d), \tag{5}$$

which is discussed later in Sec. III-B.

Since the hip base reference frame $\mathcal{F}_{hb}$ is located in a certain orientation with respect to the robot torso to allow for a collision free arrangement of the individual actuators (1–4), the hip follower frame $\mathcal{F}_{hf}$ of the tool platform must compensate for the initial orientation of the SPM base platform. Thus, as a measure to orient the leg plane upright—which means that leg and floor planes are orthogonal towards each other with $E_{L0} \perp E_F$—a target orientation is constructed by:

$$ {}^{ee}\hat{\boldsymbol{e}}_y = [0, 0, 1]^T, \tag{6}$$

$$ {}^{ee}\hat{\boldsymbol{e}}_z = \left({}^{ee}_{hb}\boldsymbol{Q}_i \cdot [0, 0, 0, 1]^T\right)_{(1:3)}, \tag{7}$$

$$ {}^{ee}\hat{\boldsymbol{e}}_x = {}^{ee}\hat{\boldsymbol{e}}_y \times {}^{ee}\hat{\boldsymbol{e}}_z, \tag{8}$$

which is combined to ${}^{ee}_{hb*}\boldsymbol{R} = \left[{}^{ee}\hat{\boldsymbol{e}}_x, {}^{ee}\hat{\boldsymbol{e}}_y, {}^{ee}\hat{\boldsymbol{e}}_z\right]^T$. Fig. 5 depicts both frames $\mathcal{F}_{hb}$ and $\mathcal{F}_{hb*}$. As a result, we express vector ${}^{hb}\boldsymbol{p}_i$ with respect to the target orientation:

$$ {}^{hb*}\boldsymbol{p} = {}^{hb*}_{ee}\boldsymbol{R} \cdot {}^{ee}_{hb}\boldsymbol{R} \cdot {}^{hb}\boldsymbol{p}. \tag{9}$$

Thus, with the known values for l_0, l_1 and d, the angles inside the leg triangle can be computed by the trigonometric equation, applying the law of cosines:

$$ \alpha_0 = \operatorname{acos}\left(\frac{l_0^2 + d^2 - l_1^2}{2 \cdot l_0 \cdot d}\right), \tag{10}$$

and similarly:

$$ \alpha_1 = \operatorname{acos}\left(\frac{l_0^2 + l_1^2 - d^2}{2 \cdot l_0 \cdot l_1}\right), \tag{11}$$

which yields the desired knee joint angle that was required as part of the general leg inverse kinematics solution.

2) HIP JOINT GENERAL KINEMATICS

Consequently, the hip joint orientation ${}^{hb}_{hf}\boldsymbol{R}$ is derived in the following. Regarding Fig. 5, angles β and γ follow with:

$$ \beta = \operatorname{atan}\left(\frac{{}^{hb*}p_x}{{}^{hb*}p_y}\right), \tag{12}$$

and:

$$ \gamma = \operatorname{atan2}\left(\operatorname{sgn}\left({}^{hb*}p_y\right)\sqrt{{}^{hb*}p_x^2 + {}^{hb*}p_y^2}, {}^{hb*}p_z\right). \tag{13}$$

The distinction between the atan and atan2 functions was applied to prevent the leg from accessing mechanically implausible postures at certain target values ${}^{hb*}\boldsymbol{p}$. Then, the matrix:

$$ {}^{hb*}_{hf}\boldsymbol{R} = \boldsymbol{R}_z(-\beta)\boldsymbol{R}_x(-\alpha_0 - \gamma - \lambda_7) \tag{14} $$

is calculated by the angle–axes–rotation matrices $\boldsymbol{R}_x$ and $\boldsymbol{R}_z$, expressing the transformation between the tool platform and the target frame. The non-constant value $\lambda_7 \neq const$ is an adjustment parameter that must be applied as an offset angle between the upper leg axis and the vertical axis of the tool platform, which is a consequence of $l_0 \neq const$. Noticeably, the axis of rotation applied through matrix $\boldsymbol{R}_x$ is colinear with axis $\hat{\boldsymbol{c}}_3$ of the underlying universal joint mechanism that supports the hip joint; hence, axis $\hat{\boldsymbol{c}}_3$ is always perpendicular to the leg plane E_{L0}. Combined with previous matrices, this yields the hip target orientation with respect to the robot torso frame:

$$ {}^{ee}_{hf}\boldsymbol{R} = \left({}^{hb*}_{ee}\boldsymbol{R}_i\right)^T \cdot {}^{hb*}_{hf}\boldsymbol{R}. \tag{15} $$

Finally, the required hip rotation matrix ${}^{hb}_{hf}\boldsymbol{R}^*$ is derived by:

$$ {}^{hb}_{hf}\boldsymbol{R}^* = \boldsymbol{R}_n(\eta, {}^{hb}\boldsymbol{p} \cdot \|{}^{hb}\boldsymbol{p}\|^{-1}) \cdot ({}^{ee}_{hb}\boldsymbol{R})^T \cdot {}^{ee}_{hf}\boldsymbol{R}, \tag{16} $$

with η denoting the leg tilt angle and $\boldsymbol{R}_n$ expressing the general angle–axis–rotation matrix with the arguments rotation angle and normalized rotation axis. Thus, with $\eta = 0$, the leg is kept at an upright orientation. Importantly, the rotation of the leg by η around axis ${}^{hb}\boldsymbol{p}$ represents a functionally redundant DOF, as it allows the leg to alter its posture without actually changing the position of the foot tip $\boldsymbol{p}$.

However, due to the additional spring DOF expressed by angle φ_s of the leg mechanism, the actual orientation of the tool platform is required to be adjusted by:

$$ {}^{hb}_{hf}\boldsymbol{R} = {}^{hb}_{hf}\boldsymbol{R}^* \cdot \boldsymbol{R}_x(\varphi_s), \tag{17} $$

which yields the hip orientation matrix for the general robot inverse kinematics.

B. LEG PLANE INVERSE KINEMATICS

In this section, the inverse kinematics of the leg mechanism is derived. First, the slider position q_{sl} inside the leg plane is calculated. Afterwards, the mapping between the slider position in the leg plane and the actuator (4) joint coordinate θ_4, which is located in the robot torso, is portrayed.

1) LEG SLIDER POSITION KINEMATICS

Fig. 6 depicts the mechanical structure of the leg. The inverse kinematics of the internal leg mechanism can be considered as a two-dimensional problem; thus, the geometrical relationships of the mechanism can be represented by simple trigonometric expressions. In this regard, (18) – (22) express four main non-constant triangles, which describe the posture

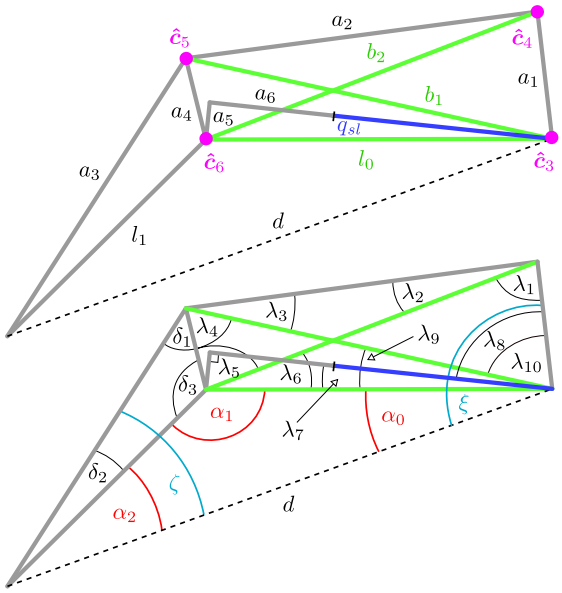

FIGURE 6. Geometry of lengths and angles inside the leg plane. For readability, the image does not represent the actual dimensions of the mechanical parts. Elements l_1 and a_1–a_6 are constant and independent of the leg posture. Green lines (b_1, b_2, l_0) depict variable lengths. The blue line (q_{sl}) refers to the length altered by the actuated slider mechanism.

of the leg:

$$ l_0^2 = l_1^2 + d^2 - 2\,l_1\,d\cos(\alpha_2), \tag{18} $$
$$ b_1^2 = a_3^2 + d^2 - 2\,a_3\,d\cos(\alpha_2 + \delta_2), \tag{19} $$
$$ a_4^2 = l_0^2 + b_1^2 - 2\,l_0\,b_1\cos(\lambda_9), \tag{20} $$
$$ a_2^2 = b_1^2 + a_1^2 - 2\,b_1\,a_1\cos(\lambda_{10}), \tag{21} $$
$$ a_5 = l_0\sin\lambda_7, \quad \text{with:} \quad \lambda_7 = \lambda_8 - \lambda_9 - \lambda_{10}. \tag{22} $$

All variables denoted with the symbols a and δ are constant and known parameters, while symbols b and λ indicate variable parameters. The value λ_8 is given by the sum of a constant δ_L and the measured spring DOF angle φ_s:

$$ \lambda_8 = \delta_L - \varphi_s, \tag{23} $$

with $\varphi_s \in [-8°, +8°]$. Thus, leg compression deforms the mechanical structure by altering angle φ_s. For a given distance value d, this is essentially a determined system composed of five equations and five unknowns (l_0, b_1, α_2, λ_9, λ_{10}).

Remarkably however, due to the length of one side of the 4-bar linkage being unknown, the derivation of a closed-form solution is not feasible, which is in contrast e.g. to the related and well known, yet more simple 4R planar linkage with determined parameters. Hence, as (18) – (22) cannot be rearranged directly to yield a closed-form solution, instead, the application of a numerical approach e.g. by the Matlab `vpasolve` algorithm [52] yields a possible solution. This then allows to derive the slider position by:

$$ q_{sl} = l_0\cos(\lambda_7) - a_6. \tag{24} $$

Notably, the geometrical representation of the problem allows for multiple solutions, which is the case if the triangles in

Fig. 6 are flipped, as this is possible without actually violating (18) – (22). Thus, even more restricting conditions could be applied. However, this is omitted here, as the solution for the inverse kinematics is continuous and fully defined without further conditions, if the mechanism is moved from a known initial arrangement. Still, a numeric solution based on (18) – (22) requires an initial guess close to a mechanically valid solution, which can be provided by virtual measurements taken from the CAD assembly model of the robot. A narrowly spanned search window then yields a working condition for a numerical solution to be sufficient.

Alternatively, a suitably more robust solution can be obtained by finding the roots of f_D, with the function f_D expressing the signed distance between the connection points of the revolute knee and slider joints at axis $\hat{\boldsymbol{c}}_6$, defined by:

$$f_D(\zeta, d) = \operatorname{sgn}(\boldsymbol{q} \cdot \boldsymbol{r}) \left\| \frac{\boldsymbol{q} \cdot \boldsymbol{r}}{\boldsymbol{q}} \right\| + a_5. \tag{25}$$

For any valid combination of target distance $d \in (0, l_1 + \max(l_0)]$ and angle $\zeta \in (\alpha_2, \pi + \alpha_2)$ it holds $f_D(\zeta, d) = 0$, representing a uniquely attainable leg posture.

Vectors $\boldsymbol{q}$ and $\boldsymbol{r}$ are defined with respect to the local Cartesian x-y-reference system. By definition, the reference frame obeys to an orientation that it always holds $\boldsymbol{p} = -d\,\hat{\boldsymbol{e}}_x$ with the position of the foot tip $\boldsymbol{p}$. Vector $\boldsymbol{r}$ represents the direction towards the knee-slider joint axis $\hat{\boldsymbol{c}}_6$ and vector $\boldsymbol{q}$ the direction perpendicular to the slider side q_{sl}. Thus, the vectors are constructed via:

$$\boldsymbol{r} = (l_1 \cos(\zeta - \delta_2) - d)\,\hat{\boldsymbol{e}}_x + l_1 \sin(\zeta - \delta_2)\,\hat{\boldsymbol{e}}_y, \tag{26}$$

$$\boldsymbol{q} = \sin(\xi - \lambda_8)\,\hat{\boldsymbol{e}}_x + \cos(\xi - \lambda_8)\,\hat{\boldsymbol{e}}_y. \tag{27}$$

Angle ξ is defined depending on d and ζ by:

$$\xi = \operatorname{acos}\left(\frac{c_1 - b_1^2}{c_2\, b_1}\right) + \operatorname{acos}\left(\frac{c_3 - b_1^2}{c_4\, b_1}\right), \tag{28}$$

with the parameters:

$$\begin{aligned} c_1 &= a_2^2 - a_1^2, \quad & c_2 &= -2a_1, \\ c_3 &= a_3^2 - d^2, \quad & c_4 &= -2\,d, \end{aligned} \tag{29}$$

and the length b_1 being:

$$b_1 = \|(a_3 \cos(\zeta) - d)\hat{\boldsymbol{e}}_x + a_3 \sin(\zeta)\hat{\boldsymbol{e}}_y\|. \tag{30}$$

Essentially, (28) captures the kinematics of the leg convex hull geometry, as depicted in Fig 6. Finally, the position of the slider inside the leg mechanism can be determined simply by:

$$q_{sl} = \sqrt{l_0^2 - a_5^2} - a_6, \tag{31}$$

where the length of the upper leg l_0—recalling (5)—follows with:

$$l_0 = f_L(d) = \|\boldsymbol{r}(\zeta, d)\|, \tag{32}$$

which is the solution to the leg planar inverse kinematics problem.

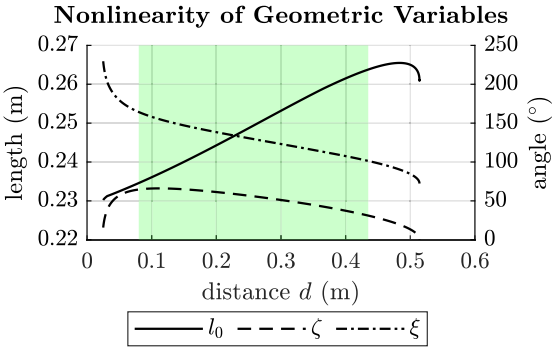

FIGURE 7. Nonlinear relationship of the upper leg length l_0 and distance d between hip centre and foot tip. Values outside of the green region are not physically attainable due to mechanical limitations of the model.

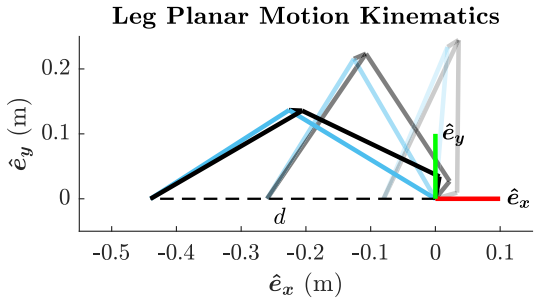

FIGURE 8. Three different postures of the leg for $d = 0.08$ m, $d = 0.26$ m and $d = 0.44$ m. Blue lines represent the sides l_0 and l_1 of the leg.

a: RESULTS

Fig. 7 depicts the variability of the length l_0 of the upper leg over the distance d between hip centre and foot point. The diagram shows that the upper leg has a maximum length variance of approximately 3.5 cm between its lower and upper workspace boundary. However, due to joint range limitations, the mechanically feasible motion is bounded to $d \in [0.080\text{ m}, 0.435\text{ m}]$. Crucially, this limitation prevents the leg mechanism to adapt to singular postures, which may degrade the conditioning of the mechanism drastically. This is visually depicted in the diagram, as the change of rate of the curvatures increases noticeably in the regions below and above the mechanical limits that hold for the distance d. The solution was implemented as a look-up table in the robot controller software for further usage.

The remaining geometry is easily expressed by similar trigonometrical equations, as shown in the appendix (Sec. A), which is required to solve for the additional joint coordinates of all passive joints inside the leg plane. Consequently, Fig. 8 shows different postures of the leg based on the actual model measurements, which are listed in Table 2 for reference.

2) SPRING DOF KINEMATICS

As the leg mechanism contains a four-bar linkage, composed of the links with the sides l_0, a_1, a_2, a_4 and the joint axes $\hat{\boldsymbol{c}}_3$, $\hat{\boldsymbol{c}}_4$, $\hat{\boldsymbol{c}}_5$, $\hat{\boldsymbol{c}}_6$, the robot is able to react compliantly to impacts or

TABLE 2. Measurements of the leg mechanism, depicting constant parameters. Note that $\delta_3 > \pi$ based on the actual model dimensions compared to Fig. 6, resulting in the lower leg triangle being flipped over.

Var.	Value	Var.	Value	Var.	Value
δ_1	$-32.65°$	a_1	0.035 m	a_5	0.007 m
δ_2	$-2.46°$	a_2	0.235 m	a_6	0.181 m
δ_3	$215.11°$	a_3	0.271 m	l_1	0.254 m
δ_L	$60.00°$	a_4	0.020 m	–	–

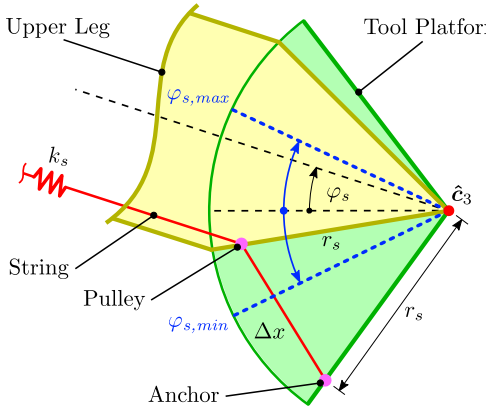

FIGURE 9. Kinematics of the spring DOF between tool platform and upper leg. The black dashed lines show the respective part symmetry axes. Blue lines depict the maximum range of motion for the spring DOF, expressed by rotation angle φ_s around axis $\hat{c}_3$. A spring with stiffness k_s pulls the parts via a string into the condition $\varphi_s = \varphi_{s,min}$.

external forces by allowing the variation of angle φ_s as the leg gets compressed. In this regard and according to Fig. 9, with a string attachment radius of $r_s = 40$ mm, the geometry of the spring implementation yields:

$$\varphi_s = \varphi_{s,min} + \operatorname{acos}\left(1 - \frac{\Delta x^2}{2r_s^2}\right), \tag{33}$$

where Δx is the actual elongation of the physical spring, located inside the upper leg.

Interestingly, the motion of the spring slot $\varphi_s \in [-8°, +8°]$ and the spring elongation $\Delta x \in [0, 11.13\text{ mm}]$ reveals a highly linear relationship. In this sense, one can show that a linear regression approximates (33) in the specified intervals by:

$$\varphi_s \approx 25.07\Delta x - 0.14, \tag{34}$$

with a minor root mean squared error of approximately $E_{rmse} \approx 1.03 \cdot 10^{-4}$.

a: RESULTS

Fig. 10 depicts the kinematics of the spring DOF in the case that both the slider DOF and the hip DOF are kept constant; thus, it holds $\theta_k = \text{const}$, $q_{sl} = \text{const}$ and $\theta_{b,1-3} = \text{const}$. Consequently, the figure expresses the motion of the foot tip due to the compression of the leg—only altering the spring DOF angle φ_s—for different initial distances d. Note that the initial design of the leg was motivated by balancing the factors

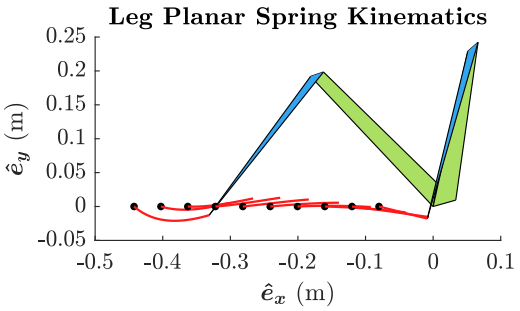

FIGURE 10. Motion of the foot tip due to variation of φ_s, shown as red lines. Black dots depict the initially non-compressed posture of the leg with $\varphi_s = \varphi_{s,min}$.

dexterity and distance to singularities, while still keeping a fairly colinear motion of the foot tip toward the virtual foot-hip vector $-d\hat{e}_x$ as the leg gets compressed. Hence, Fig. 10 shows that the foot stays in a narrow region towards $f(x) = -x\hat{e}_x$ as a measure to reduce the possibly problematic influence of lateral motion during leg compression phases.

3) KNEE ACTUATOR KINEMATICS

In the robot model, the leg mechanism is serially connected to the hip manipulator end-effector. However, the actuator that drives the knee joint is actually located inside the robot torso. Thus, the kinematics between the linear motion of the slider q_{sl} on axis $\hat{\boldsymbol{c}}_7$ and the actuator axis $\hat{\boldsymbol{u}}_4$ is considered in the following. In general, the transmission of rotation is realized by a constant velocity bendable transmission axis, which is then transformed into linear motion by a screw joint. In this regard, considering that the hip base actuator velocity holds $\dot{\boldsymbol{\theta}}_b = \boldsymbol{0}$, the systemic relationship between motor input and slider output velocity is only determined by the screw pitch, which is simply:

$$\theta_4^* = 2\pi \frac{q_{sl}}{p}, \tag{35}$$

with the screw pitch of $p = 10$ mm per rotation.

4) HIP MOTION DISTURBANCE KINEMATICS

However, in the general case $\dot{\boldsymbol{\theta}}_b \neq \boldsymbol{0}$ and due to the RRR joint support structure inside the hip mechanism, composed of the axes $\hat{\boldsymbol{c}}_1, \hat{\boldsymbol{c}}_2$ and $\hat{\boldsymbol{c}}_3$, with the knee actuator being fixed to the proximal part of the universal joint, spherical motion of the hip joint yields a constrained rotation of the knee actuator itself around axis $\hat{\boldsymbol{c}}_1$. Consequently, this induced motion of the knee axis must be compensated at all times in order to keep the slider position q_{sl} at its desired location. Similarly, any tilt motion of the leg by η around its redundant DOF with axis ${}^{hb}\boldsymbol{p}$ must be compensated additionally.

In this regard, the orientation of the upper leg with respect to the hip base platform is expressed by the matrix ${}^{hb}_{hf}\boldsymbol{R}^*$, as noted in (16). However, as the axes $\hat{\boldsymbol{c}}_1$, $\hat{\boldsymbol{c}}_2$ and $\hat{\boldsymbol{c}}_3$ of the RRR joint support structure are perpendicular to each others neighbour at all times, meaning $\hat{\boldsymbol{c}}_1 \cdot \hat{\boldsymbol{c}}_2 = \hat{\boldsymbol{c}}_2 \cdot \hat{\boldsymbol{c}}_3 = 0$, we can express ${}^{hb}_{hf}\boldsymbol{R}^*$ as a series concatenation of basic

rotation matrices:

$$ {}^{hb}_{hf}\boldsymbol{R}^{*} = \boldsymbol{R}_z(\alpha_z)\boldsymbol{R}_y(\alpha_y)\boldsymbol{R}_x(\alpha_x) = \left[\boldsymbol{r}_1\ \boldsymbol{r}_2\ \boldsymbol{r}_3\right], \tag{36} $$

with the column vectors:

$$ \boldsymbol{r}_1 = \left[\mathrm{c}(\alpha_y)\mathrm{c}(\alpha_z),\ \mathrm{c}(\alpha_y)\mathrm{s}(\alpha_z),\ -\mathrm{s}(\alpha_y)\right]^T, \tag{37} $$

$$ \boldsymbol{r}_2 = \begin{bmatrix} \mathrm{c}(\alpha_z)\mathrm{s}(\alpha_x)\mathrm{s}(\alpha_y) - \mathrm{c}(\alpha_x)\mathrm{s}(\alpha_z) \\ \mathrm{c}(\alpha_x)\mathrm{c}(\alpha_z) + \mathrm{s}(\alpha_x)\mathrm{s}(\alpha_y)\mathrm{s}(\alpha_z) \\ \mathrm{c}(\alpha_y)\mathrm{s}(\alpha_x) \end{bmatrix}, \tag{38} $$

$$ \boldsymbol{r}_3 = \begin{bmatrix} \mathrm{c}(\alpha_x)\mathrm{c}(\alpha_z)\mathrm{s}(\alpha_y) + \mathrm{s}(\alpha_x)\mathrm{s}(\alpha_z) \\ -\mathrm{c}(\alpha_z)\mathrm{s}(\alpha_x) + \mathrm{c}(\alpha_x)\mathrm{s}(\alpha_y)\mathrm{s}(\alpha_z) \\ \mathrm{c}(\alpha_x)\mathrm{c}(\alpha_y) \end{bmatrix}. \tag{39} $$

Thus, equivalent to a general ZYX-Euler decomposition as shown in [28], the angle α_y can be determined by:

$$ \alpha_y = \mathrm{asin}\left(-{}^{hb}_{hf}\boldsymbol{R}^{*}_{(3,1)}\right). \tag{40} $$

Due to mechanical constraints of the universal joint for axis $\hat{\boldsymbol{c}}_2$, it holds $\alpha_y \in (-\pi/2, \pi/2)$, and thus always $\cos(\alpha_y) \neq 0$. Consequently, with:

$$ \cos\alpha_y \cos\alpha_z = {}^{hb}_{hf}\boldsymbol{R}^{*}_{(1,1)}, \tag{41} $$

$$ \cos\alpha_y \sin\alpha_z = {}^{hb}_{hf}\boldsymbol{R}^{*}_{(2,1)}, \tag{42} $$

it follows that:

$$ \frac{{}^{hb}_{hf}\boldsymbol{R}^{*}_{(2,1)}}{{}^{hb}_{hf}\boldsymbol{R}^{*}_{(1,1)}} = \tan\alpha_z, \tag{43} $$

which delivers the angle α_z corresponding to the $\hat{\boldsymbol{c}}_1$-axis.

Hence, with the rotation of the lead screw around axis $\hat{\boldsymbol{c}}_{8,9}$—colinear with the prismatic slider axis $\hat{\boldsymbol{c}}_7$—being kept constant and with $\hat{\boldsymbol{c}}_{8,9}$ being perpendicular to the $\hat{\boldsymbol{c}}_3$-axis, as depicted in Fig. 6, the rotation of the upper leg around the hip centre point naturally results in a rotation around the proximal support joint axis $\hat{\boldsymbol{c}}_1$ by α_z. Thus, α_z can be exploited as an offset to compensate for the current leg orientation regarding the knee actuator axis angle θ_4, which consequently must be applied to axis $\hat{\boldsymbol{u}}_4$ in order to keep q_{sl} at its desired value. Therefore, combined with (35), the actuator angular position θ_4 is defined as:

$$ \theta_4 = \mathrm{atan}\left(\frac{{}^{hb}_{hf}\boldsymbol{R}^{*}_{(2,1)}}{{}^{hb}_{hf}\boldsymbol{R}^{*}_{(1,1)}}\right) + \theta^{*}_4. \tag{44} $$

C. HIP INVERSE KINEMATICS: SPM GEOMETRICAL SOLUTION

Since the general inverse kinematics of the top-level system are solved at this point, now the kinematics of the underlying SPM subsystem have to be taken into account. Therefore, considering a known orientation of the SPM, expressed by the 3-by-3 orthogonal matrix ${}^{hb}_{hf}\boldsymbol{R}$, the solution for the actuator joint angles $\theta_{b,j}$, according to the general layout of the mechanism is required, see Fig. 4.

Considering the vectors $\hat{\boldsymbol{u}}_j$ fixed to the base platform in the reference frame $\mathcal{F}_{hb,i}$ and the vectors $\hat{\boldsymbol{w}}_j$ fixed to the tool platform (end-effector) in the frame $\mathcal{F}_{hf,i}$, the transformation matrix between those frames reads ${}^{hf}_{hb}\boldsymbol{R}_i$, according to Fig. 11. Thus, ${}^{hf}_{hb}\boldsymbol{R}_i$ represents the transformation matrix of the virtual spherical center joint, connecting hip joint base (hb) and hip joint follower (hf) frames. The matrix ${}^{hf}_{hb}\boldsymbol{R}_i = \boldsymbol{I}$ with the identity matrix $\boldsymbol{I}$ represents the initial configuration of the manipulator, which aligns base and follower frame. To be more specific, based on the optimal design of the SPM that is derived in [38], in the isotropic case ${}^{hf}_{hb}\boldsymbol{R}_i = \boldsymbol{I}$, which is used here as the manipulator ideal configuration, each axis $\hat{\boldsymbol{u}}_j$ has a corresponding axis $\hat{\boldsymbol{w}}_{j+1}$ oriented anti-parallel. Thus, the floor projected angle in Fig. 11 equals $\pi/3$, while neighbouring axes in the base and tool platform are oriented by $\pi/2$ towards each other.

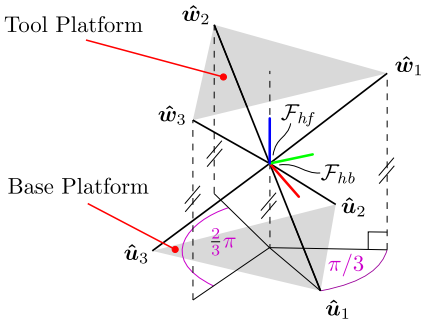

FIGURE 11. Initial configuration of base- and tool-vectors of the SPM. Hip base and follower frames of the virtual spherical joint align in the manipulator isotropic pose.

The angular position of the actuator or base axes $\hat{\boldsymbol{u}}_j$ is denoted with the angles $\theta_{b,j}$. Angles around the link and tool axes are denoted with $\theta_{l,j}$ and $\theta_{t,j}$, respectively. A set of angles for all linkages $j = 1, 2, 3$ is combined to the vectors $\boldsymbol{\theta}_b$, $\boldsymbol{\theta}_l$ and $\boldsymbol{\theta}_t$.

1) CONCEPT

In the following, the solution to the inverse kinematics of the SPM based on spherical trigonometry is derived. Due to the purely rotational motion of all parts of the SPM around a common centre point, it is possible to project the geometry of the mechanism onto a unit sphere, without changing the properties of the mechanical model. Hence, the spherical motion does not depend on the actual distance of the links to the centre of the mechanism. Therefore, the actual shape and distance of each link to the centre of the mechanism has to be considered only regarding the dexterity for a physically realized manipulator as a measure to prevent internal collisions between parts. Thus, the problem to solve for the inverse kinematics of the spherical parallel mechanism is reduced to a simple geometrical expression that can be approached and analysed via the application of spherical trigonometry.

2) MATHEMATICAL DERIVATION

A major part that yields to the solution of the inverse kinematics problem is based on the mathematical properties of the unit sphere with radius $r = 1$. Since each joint axis of

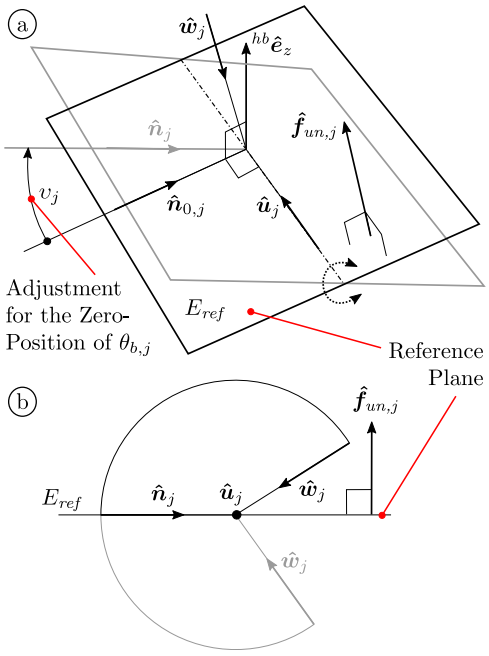

FIGURE 12. (a) Reference plane E_{ref} spanned by $\hat{n}_j$ and $\hat{u}_j$. Vector $\hat{u}_j$ also equals the rotation axis of the reference plane with rotation angle υ_j. (b) Side view of plane E_{ref}. A flipped spherical triangle occurs if $\hat{w}_j$ moves beyond the reference plane.

the SPM intersects in the common centre of the mechanism, all axes correspond to vectors orthogonal to the surface of a sphere. Hence, angles between axes—that are intersecting at the centre of the unit sphere—are identical to the lengths of the arcs spanning between these axes on the surface of the unit sphere, which is a property necessary for the trigonometric solution presented.

In the following, a vector $^{hb}\boldsymbol{x}$ is expressed with respect to the $\mathcal{F}_{hb}$ reference frame. However, for the purpose of a shorter notation, and if not stated otherwise, it is assumed that any vector $\boldsymbol{x}$ without carrying a label to a specific reference frame is also defined with respect to the $\mathcal{F}_{hb}$ system.

a: DEFINITION OF THE REFERENCE PLANE

At first, a fixed point of reference for the actuator angular position expressed by the angles $\theta_{b,j}$ has to be defined. Therefore, a plane E_{ref} locally fixed to the base platform and spanned by the actuator axes $\hat{\boldsymbol{u}}_j$ and a vector $\hat{\boldsymbol{n}}_j$ perpendicular to the actuator axes is defined. In addition, the orientation of this plane around axis $\hat{\boldsymbol{u}}_j$ determines the shape of the further used spherical triangles. For this analysis, a perpendicular relation between $\hat{\boldsymbol{n}}_j$ and the $^{hb}\hat{\boldsymbol{e}}_z$ direction of the hip base reference frame was chosen. Fig. 12a shows the plane E_{ref}, intersecting with the origin of the hip base reference frame.

In this approach, each angle inside the further used spherical triangles—spanned between the vectors $\hat{\boldsymbol{n}}_j$, $\hat{\boldsymbol{u}}_j$ and $\hat{\boldsymbol{w}}_j$—is not allowed to exceed π, because otherwise, a flip occurs, and the spherical triangle takes place on the opposite site of the reference plane. Hence, as long as the tool vector $\hat{\boldsymbol{w}}_j$ stays above the plane E_{ref}, defined by:

$$E_{ref} : \boldsymbol{x} \cdot (\hat{\boldsymbol{n}}_j \times \hat{\boldsymbol{u}}_j) = 0, \tag{45}$$

with an arbitrary vector $\boldsymbol{x}$ inside the plane surface, which yields the condition:

$$(\hat{\boldsymbol{n}}_j \times \hat{\boldsymbol{u}}_j) \cdot \hat{\boldsymbol{w}}_j = \hat{\boldsymbol{f}}_{un,j} \cdot \hat{\boldsymbol{w}}_j < 0, \tag{46}$$

the geometrical solution is possible. To account for a flipped spherical triangle, which can occur at large twist or tilt motions of the SPM, a factor $f_{flip,un,j}$ is introduced:

$$f_{flip,un,j} := \begin{cases} +1 & \text{for} \hat{\boldsymbol{f}}_{un,j} \cdot \hat{\boldsymbol{w}}_j < 0 \\ -1 & \text{for} \hat{\boldsymbol{f}}_{un,j} \cdot \hat{\boldsymbol{w}}_j \geq 0, \end{cases} \tag{47}$$

covering both possible postures of the manipulator for the further solution. Importantly, $\hat{\boldsymbol{w}}_j$ is expressed with respect to the $\mathcal{F}_{hb}$ reference system. Fig. 12b shows both cases for the spherical triangle regarding the relation to the reference plane.

b: DEFINITION OF THE REFERENCE VECTOR

For simplicity, accounting for both cases as stated with (47) may not be required, if the angle between $\hat{\boldsymbol{n}}_j$ and $\hat{\boldsymbol{e}}_z$ is altered to align the solution space to the typical workspace of the manipulator. This might be possible regarding a real world manipulator, since the reachable workspace may be limited by mechanical constraints of the mechanism itself. That means by rotating the plane around $\hat{\boldsymbol{u}}_j$ by altering $\hat{\boldsymbol{n}}_j$, the workspace borders, in which a solution can be found, can be shifted towards the individual movement requirements of the SPM. According to Fig. 12a, the base reference vector $\hat{\boldsymbol{n}}_{0,j}$ can be derived by:

$$\hat{\boldsymbol{n}}_{0,j} = \frac{\boldsymbol{n}_{0,j}}{\|\boldsymbol{n}_{0,j}\|} \quad \text{with} \quad \boldsymbol{n}_{0,j} = \hat{\boldsymbol{u}}_j \times \hat{\boldsymbol{e}}_z, \tag{48}$$

if $\hat{\boldsymbol{u}}_j \nparallel \hat{\boldsymbol{e}}_z$. Alternatively, it is possible to define $\hat{\boldsymbol{n}}_{0,j}$ according to Fig. 13b:

$$\hat{\boldsymbol{n}}_{0,j} = -\sin\delta_j \hat{\boldsymbol{e}}_x + \cos\delta_j \hat{\boldsymbol{e}}_y, \tag{49}$$

which satisfies for $\hat{\boldsymbol{n}}_j \cdot \hat{\boldsymbol{u}}_j = 0$. In addition, with the angle-axis rotation matrix $\boldsymbol{R}_n$, the vector $\hat{\boldsymbol{n}}_j$ is optionally rotated to shift the solution space of the SPM:

$$\hat{\boldsymbol{n}}_j := \begin{cases} \boldsymbol{R}_n(\upsilon_j, \hat{\boldsymbol{u}}_j) \cdot \hat{\boldsymbol{n}}_{0,j} & \text{for } \upsilon_j \neq 0 \\ \hat{\boldsymbol{n}}_{0,j} & \text{for } \upsilon_j = 0, \end{cases} \tag{50}$$

which simply leads to vales $\boldsymbol{\theta}_b$ containing a constant offset, redefining the zero-position of the base angles.

c: CONSTRUCTION OF THE GENERAL SPM AXES

As can be seen in Fig. 13a, the actuator angle $\theta_{b,j}$ is measured around the actuator axes between plane and proximal link. In this case, the final configuration of the leg structure is already assumed to take the right-branch-solution, which relates to the specific mechanical layout of the SPM,

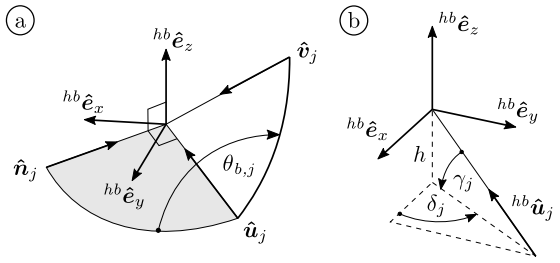

FIGURE 13. (a) Reference plane for the actuator angle $\theta_{b,j}$. For this analysis it holds $\hat{n}_j \perp {}^{hb}\hat{e}_z$. (b) Construction of the actuator axis $\hat{u}_j$.

as discussed later. Based on Fig. 13b, the unit vector $\hat{\boldsymbol{u}}_j$ can be expressed as:

$$\hat{\boldsymbol{u}}_j = -\cos\gamma_j\cos\delta_j\hat{\boldsymbol{e}}_x - \cos\gamma_j\sin\delta_j\hat{\boldsymbol{e}}_y + \sin\gamma_j\hat{\boldsymbol{e}}_z \tag{51}$$

with the vertical angle γ_j and with the horizontal orientation angle δ_j.

For the general SPM, with $\hat{\boldsymbol{u}}_j$ known, constructing the vector $\hat{\boldsymbol{v}}_j$ based on the calculated angular position $\theta_{b,j}$ requires a simple concatenation of rotation matrices:

$$\hat{\boldsymbol{v}}_j = \boldsymbol{R}_{b,j} \cdot \boldsymbol{R}_z(\theta_{b,j}) \cdot \boldsymbol{R}_y(l_{uv,j}) \cdot \hat{\boldsymbol{e}}_z, \tag{52}$$

with the geometrically constructed matrix:

$$\boldsymbol{R}_{b,j} = \left[\hat{\boldsymbol{n}}_j, -\hat{\boldsymbol{f}}_{un,j}, \hat{\boldsymbol{u}}_j\right], \tag{53}$$

representing an orthogonal reference frame fixed to the base platform, expressed by the three vectors $\hat{\boldsymbol{n}}_j$, $-\hat{\boldsymbol{f}}_{un,j}$ and $\hat{\boldsymbol{u}}_j$ that were derived before, and the vector $\hat{\boldsymbol{e}}_z = [0, 0, 1]^T$. Similarly, the tool vectors $\hat{\boldsymbol{w}}_j$ can be constructed by the series concatenation of the respective transformation matrices of the linkages. Thus, it follows:

$$\hat{\boldsymbol{w}}_j = \boldsymbol{R}_{b,j} \cdot \boldsymbol{R}_z(\theta_{b,j}) \cdot \boldsymbol{R}_y(l_{uv,j}) \cdot \boldsymbol{R}_z(\theta_{l,j}) \cdot \boldsymbol{R}_y(-l_{vw,j}) \cdot \hat{\boldsymbol{e}}_z. \tag{54}$$

d: CONSTRUCTION OF THE OPTIMAL SPM AXES

As shown in [38], there exists an optimal configuration for the SPM regarding the resulting accuracy, and the relationships of velocity and torque of the mechanism. Due to the properties of this specific configuration, the construction of the axes $\hat{\boldsymbol{u}}_j$, $\hat{\boldsymbol{v}}_j$ and $\hat{\boldsymbol{w}}_j$ simplifies noticeably.

Thus, the optimal configuration of the SPM as shown in [38] requires an angle of $\pi/2$ between neighbouring axes $\hat{\boldsymbol{u}}_j$, fixed to the base platform, and tool axes $\hat{\boldsymbol{w}}_j$, fixed to the tool platform. In this specific case, the set of base axes ($\hat{\boldsymbol{u}}_1$, $\hat{\boldsymbol{u}}_2$, $\hat{\boldsymbol{u}}_3$) and the set of tool axes ($\hat{\boldsymbol{w}}_1$, $\hat{\boldsymbol{w}}_2$, $\hat{\boldsymbol{w}}_3$) both construct a three-dimensional cartesian coordinate system, hence the orientation of the vectors $\hat{\boldsymbol{u}}_j$ and $\hat{\boldsymbol{w}}_j$ can be determined by the application of a standard rotation matrix on the central $\mathcal{F}_{hb}$ system. Hence, reusing the angles γ_j—however due to symmetry without accounting for the index j—the identical result may be obtained by defining:

$$\boldsymbol{R} = \boldsymbol{R}_y(\pi + \gamma) \cdot \boldsymbol{R}_x(5/4\,\pi). \tag{55}$$

In [74], a different, yet conceptually similar construction was used. Consequently, applying the unit vectors $\hat{\boldsymbol{e}}_x$, $\hat{\boldsymbol{e}}_y$ and $\hat{\boldsymbol{e}}_z$ on the matrix $\boldsymbol{R}$ of (55), it follow the individual vectors $\hat{\boldsymbol{u}}_j$. Thus, this yields that $\hat{\boldsymbol{u}}_j$ is the j-th column of $\boldsymbol{R}$:

$$\hat{\boldsymbol{u}}_j = (\boldsymbol{R})_{(1:3,j)}, \tag{56}$$

with the index denoting rows and columns of the matrix $\boldsymbol{R}$. Interestingly, (56) only represents a right-handed orthogonal reference frame due to the specific definition regarding the directing of the vectors $\hat{\boldsymbol{u}}_j$, pointing towards the center of the manipulator.

Alternatively, the construction with regard to (51) requires both angles δ_j and γ_j. Due to the symmetry of the system, the angle δ_j follows with:

$$\delta_j = \frac{j-1}{3}2\pi, \quad \text{with} \quad j = 1, 2, 3. \tag{57}$$

Similarly, the angle γ_j follows to:

$$\gamma_j = \operatorname{asin}(h), \tag{58}$$

with $h = \sqrt{1/3}$ as depicted in Fig. 13b being the vertical height. Notably, h can be calculated by simple trigonometric calculations, yet in this case, it is derived from the relationship:

$$\frac{1}{h^2} = \sum_{j=1}^{3} \frac{1}{\|\hat{\boldsymbol{u}}_j\|^2}. \tag{59}$$

Since the orientation of axes $\hat{\boldsymbol{u}}_j$ is equal to the shape of a trirectangular tetrahedron, (59) expresses the relationship between the altitude of the tetrahedron and the lengths of its sides, which is a trigonometric property as stated in [32, p. 41]. In the isotropic pose, the planes spanned by the arcs of the proximal and distal link are oriented orthogonal to each other, which—since it holds $l_{uv,j} = l_{vw,j} = \pi/2$—naturally yields that base and tool axes must equally retain a right-angled configuration. Consequently, each axis $\hat{\boldsymbol{u}}_j$ corresponds to an axis $\hat{\boldsymbol{w}}_j$ oriented anti-parallel in the isotropic pose. Lastly, due to the orthogonal relationship, the link axis follows with:

$$\hat{\boldsymbol{v}}_j = \hat{\boldsymbol{u}}_j \times \hat{\boldsymbol{w}}_j, \tag{60}$$

which results in neighboring link axes and base axes being aligned in the isotropic pose.

Consequently, the specific values for the axes $\hat{\boldsymbol{u}}_j$, $\hat{\boldsymbol{v}}_j$, $\hat{\boldsymbol{w}}_j$ with respect to the $\mathcal{F}_{hb}$-reference frame can be calculated and are given in Table 3. However, these values are only valid for the home posture of the optimal SPM as depicted in Fig. 21 in the appendix, which is an isotropic configuration of the manipulator, meaning that this specific posture constitutes to an ideal torque and velocity input-output-relationship of the mechanism. A MATLAB [52] example function featuring the implementation for the discussed axes construction methods is included in the supplementary materials.

TABLE 3. Values for the isotropic home configuration of the optimal SPM with $l_{uv,j} = l_{vw,j} = \pi/2$ and $\pi/2$ between neighboring base axes $\hat{u}_j$ and tool axes $\hat{w}_j$. The indexes of $\hat{v}_j$ and $\hat{w}_j$ are permuted. All values are expressed in the central $\mathcal{F}_{hb}$-frame.

Base	Link	Tool	$\hat{e}_x$	$\hat{e}_y$	$\hat{e}_z$
$\hat{u}_1$	$\hat{v}_3$	$-\hat{w}_2$	$-\sqrt{6}/3$	0	$\sqrt{3}/3$
$\hat{u}_2$	$\hat{v}_1$	$-\hat{w}_3$	$\sqrt{6}/6$	$-\sqrt{2}/2$	$\sqrt{3}/3$
$\hat{u}_3$	$\hat{v}_2$	$-\hat{w}_1$	$\sqrt{6}/6$	$\sqrt{2}/2$	$\sqrt{3}/3$

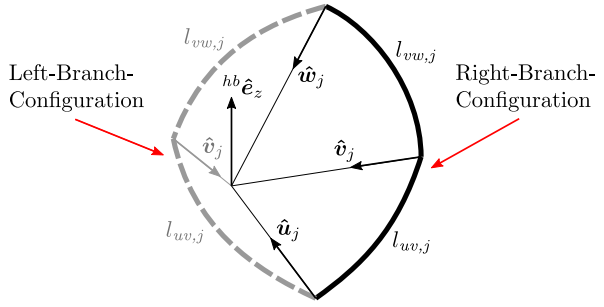

FIGURE 14. Right-branch- and left-branch-configuration for proximal and distal link j. $\hat{u}_j$ and $\hat{w}_j$ are identical for both configurations, but $\hat{v}_j$ is flipped, depicting two working modes of the SPM linkages.

e: BRANCH SELECTION

For each reachable orientation of the SPM, two possible solutions exist for the linkage structure of proximal and distal link, see Fig. 14, which represents the different working modes of the SPM. In this article, the possible configurations are distinguished by naming them as *right-branch-* and *left-branch-*configuration. Since mechanical collisions have to be avoided, each linkage of the SPM is usually kept at the same branch configuration, i.e. stays in the same working mode. Furthermore, flipping of the configuration from one to the other is usually not intended while reorienting the SPM, since this involves moving the mechanism through points of mechanical singularity. In reality, flipping the linkages is in general not possible due to the often asymmetrical mechanical design of the links themselves. However, to account for both configurations for the further solution of the inverse kinematics problem, the factor $f_{branch,j}$ is introduced:

$$f_{branch,j} := \begin{cases} +1 & \text{for the right-branch-config.} \\ -1 & \text{for the left-branch-config.,} \end{cases} \tag{61}$$

which expresses the specific mechanical layout of the manipulator. Essentially, directly including the chosen layout into the solution to the inverse kinematics results in a unique solution, as this removes the mathematical possibility for two configurations to exits in comparison to a general algebraic approach for the inverse kinematics.

f: APPLICATION OF SPHERICAL TRIGONOMETRY

Knowing the direction of the tool axis unit vector $\hat{\boldsymbol{w}}_j$ based on a given orthogonal mapping matrix ${}^{hb}_{hf}\boldsymbol{R} \in \mathbb{R}^{3\times3}$ and the unit

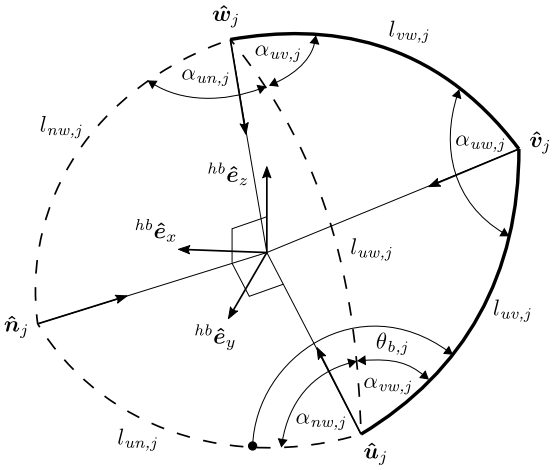

FIGURE 15. Construction of spherical triangles $(\hat{n}_j, \hat{u}_j, \hat{w}_j)$ and $(\hat{u}_j, \hat{v}_j, \hat{w}_j)$. Link arcs lengths are named by the letter l and angles inside the spherical triangles by the letter α.

vector ${}^{hf}\hat{\boldsymbol{w}}_j$ fixed to the follower frame, the target orientation can be computed:

$${}^{hb}\hat{\boldsymbol{w}}_j = {}^{hb}_{hf}\boldsymbol{R} \cdot {}^{hf}\hat{\boldsymbol{w}}_j. \tag{62}$$

The unit vector ${}^{hf}\hat{\boldsymbol{w}}_j$ is a known constant regarding its orientation inside the hip joint follower frame. Therefore, if the SPM is in its default orientation, meaning ${}^{hb}_{hf}\boldsymbol{R} = \boldsymbol{I}$ with the identity matrix $\boldsymbol{I}$, it follows that for the components of both vectors it holds ${}^{hb}w_{k,j} = {}^{hf}w_{k,j}$ with $k = 1, 2, 3$, which is useful for determining the vector in the first place.

The geometrical approach to the solution of the inverse kinematics now requires the application of spherical trigonometry on the unit sphere. Thus, by defining two spherical triangles according to Fig. 15, the cosine rule can be applied. For the first spherical triangle this holds:

$$\cos l_{vw,j} = \cos l_{uv,j} \cdot \cos l_{uw,j} + \sin l_{uv,j} \cdot \sin l_{uw,j} \cdot \cos\alpha_{vw,j}. \tag{63}$$

With the given radian of the proximal link $l_{uv,j}$ and distal link $l_{vw,j}$, the length of the connection arc $l_{uw,j}$, which is also the angle between the vectors $\hat{\boldsymbol{u}}_j$ and $\hat{\boldsymbol{w}}_j$, can be derived by:

$$l_{uw,j} = \operatorname{acos}(\hat{\boldsymbol{u}}_j \cdot \hat{\boldsymbol{w}}_j) \in [0, \pi]. \tag{64}$$

With the argument:

$$arg_{vw,j} = \frac{\cos l_{vw,j} - \cos l_{uv,j} \cdot \cos l_{uw,j}}{\sin l_{uv,j} \cdot \sin l_{uw,j}}, \tag{65}$$

(63) can be rearranged to:

$$\alpha_{vw,j} := \begin{cases} \operatorname{acos}\left(arg_{vw,j}\right) & \text{if } arg_{vw,j} \in [-1, +1] \\ \dfrac{\pi}{2} & \text{if } l_{uw,j} = \pi \vee l_{uw,j} = 0, \end{cases} \tag{66}$$

which gives the intermediate angle $\alpha_{vw,j}$. Importantly, the second case in (66) represents that axes $\hat{\boldsymbol{u}}_j$ and $\hat{\boldsymbol{v}}_j$ are

geometrically aligned, which results in a discontinuity that must be covered mathematically.

Considering the second spherical triangle, the cosine rule can be applied again:

$$\cos l_{nw,j} = \cos l_{uw,j} \cdot \cos l_{un,j} + \sin l_{uw,j} \cdot \sin l_{un,j} \cdot \cos \alpha_{nw,j}, \tag{67}$$

where the additional arcs can be derived according to Fig. 15 by:

$$l_{nw,j} = \operatorname{acos}(\hat{\boldsymbol{w}}_j \cdot \hat{\boldsymbol{n}}_j), \tag{68}$$

and with $\hat{\boldsymbol{u}}_j \perp \hat{\boldsymbol{n}}_j$ it leads to:

$$l_{un,j} = \operatorname{acos}(\hat{\boldsymbol{u}}_j \cdot \hat{\boldsymbol{n}}_j) = \frac{\pi}{2}. \tag{69}$$

Rearranging (67) and inserting (69) yields:

$$\alpha_{nw,j} := \begin{cases} \operatorname{acos}\underbrace{\left(\dfrac{\cos l_{nw,j}}{\sin l_{uw,j}}\right)}_{arg_{nw,j}} & \text{if } arg_{nw,j} \in [-1, +1] \\ \dfrac{\pi}{2} & \text{if } l_{uw,j} = \pi \vee l_{uw,j} = 0, \end{cases} \tag{70}$$

which gives the next intermediate angle $\alpha_{nw,j}$, again with the second case modelling the geometric discontinuity. Finally, the actuator angles can be computed by:

$$\theta_{b,j} = \alpha_{nw,j} \cdot f_{flip,un,j} + \alpha_{vw,j} \cdot f_{branch,j}, \tag{71}$$

which is the general solution for the inverse kinematics of the spherical parallel manipulator, derived through spherical trigonometry.

g: DEGENERATION OF THE INVERSE KINEMATICS

Two special cases have to be considered for the motion of the SPM that occur at $\hat{\boldsymbol{u}}_j \times \hat{\boldsymbol{w}}_j = 0$ and result in no explicit solution as the expressions in (66) and (70) degenerate. Here, the spherical triangles are fully expanded with $l_{uw} = \pi$ or fully collapsed with $l_{uw} = 0$, marking points of singularity for the mechanism.

In other words and mechanically speaking, $l_{uw} = \pi$ means that proximal and distal links are fully unfolded, while on the other hand $l_{uw} = 0$ means that both links are fully folded. Regarding Fig. 16, the expanded state is only possible if both vectors $\hat{\boldsymbol{u}}_j$ and $\hat{\boldsymbol{w}}_j$ are oriented in line:

$$l_{uw} = \pi, \text{ if } \hat{\boldsymbol{u}}_j \parallel -\hat{\boldsymbol{w}}_j, \tag{72}$$

and the collapsed state is only possible if both vectors are aligned:

$$l_{uw} = 0, \text{ if } \hat{\boldsymbol{u}}_j \parallel \hat{\boldsymbol{w}}_j. \tag{73}$$

This requires for the length of the linkage to hold $l_{uv} + l_{vw} = \pi$ in the first case, and $l_{uv} = l_{vw}$ in the second case. Both situations are modelled by a discontinuity with $\alpha_{nw} = \pi/2$ and $\alpha_{vw} = \pi/2$, as noted in (66) and (70).

Mechanically, both discontinuities correspond to singularity configurations of the mechanism, resulting in the free rotation of the complete linkage between base and tool platform. More specifically, the configuration of the manipulator—as determined by the second case in (66) and (70)—results in a zero velocity motion of the tool platform for a non-zero actuator velocity, which is called a serial or type 1 singularity [64, p. 180]. Crucially, this means that no torque can be transmitted between actuator and end-effector in this posture. Notably, the discontinuity expressed by (66) and (70) covers only the specific situation with the axes $\hat{\boldsymbol{u}}_j$ and $\hat{\boldsymbol{w}}_j$ being colinear, which is only one of several types of singularities that are possible regarding SPMs.

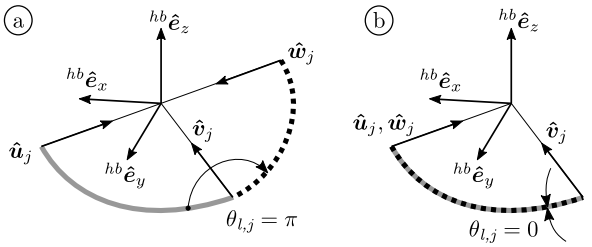

FIGURE 16. It holds $l_{uv} = l_{vw} = \pi/2$. (a) Expanded state with $\hat{\boldsymbol{u}}_j \parallel -\hat{\boldsymbol{w}}_j$. (b) Collapsed state with $\hat{\boldsymbol{u}}_j \parallel \hat{\boldsymbol{w}}_j$.

h: FINITE AND INFINITE JOINT ROTATION

In addition to the previous discussion, Fig. 16 graphically visualizes one additional property of the manipulator geometry. Despite being in general observed in parallel manipulators in the case that joint axes align, the geometrical approach makes the motion capability of the base actuator axis in singularity postures visually apparent, which results in either only finite or infinite rotation. Hence, the implications of the solvability of the inverse kinematics with respect to singularity configurations will be discussed in the following.

Since the extreme conditions of the fully expanded (unfolded) or collapsed (folded) manipulator with $\hat{\boldsymbol{u}}_j \parallel -\hat{\boldsymbol{w}}_j$ and $\hat{\boldsymbol{u}}_j \parallel \hat{\boldsymbol{w}}_j$ are only reachable for the case that it holds simultaneously $l_{uv} + l_{vw} = \pi$ and $l_{uv} = l_{vw}$, it is immediately obvious that a manipulator has to be designed with $l_{uv} = \pi/2$ for the proximal and $l_{vw} = \pi/2$ for the distal link to be able to support both cases and—importantly—to reach any point, located arbitrarily on a spherical surface. This result was analytically proven in [38] by analysing the mobility regions of the individual linkages.

However, a different situation is apparent if $l_{uv} \neq \pi/2$ and $l_{vw} \neq \pi/2$, yet still qualify for $\hat{\boldsymbol{u}}_j$ and $\hat{\boldsymbol{w}}_j$ being colinear, allowing for singularity configurations. In general, serial (type 1) singularities remove one DOF from the manipulator; thus, if one linkage is in a type 1 state, the SPM will only remain with two DOFs. However, two distinct behaviours can be observed for type 1 singularities at the SPM, depending on the static geometry of the linkages. Therefore, in the case (A) of $l_{uv} = l_{vw}$, but $l_{uv} + l_{vw} \neq \pi$ only one configuration per link exists that aligns $\hat{\boldsymbol{u}}_j$ and $\hat{\boldsymbol{w}}_j$, allowing the actuator axes to freely rotate the linkages infinitely. Since the axes $\hat{\boldsymbol{u}}_j$ and $\hat{\boldsymbol{w}}_j$ are parallel, this means that the linkage is folded.

Similarly (B), if $l_{uv} \neq l_{vw}$, but $l_{uv} + l_{vw} = \pi$, axes $\hat{\boldsymbol{u}}_j$ and $\hat{\boldsymbol{w}}_j$ can be aligned anti-parallel, meaning the linkage is now unfolded. This again corresponds to a singularity configuration, allowing for infinite rotation of the actuator axis. Consequently, both cases (A) and (B) allow that the actuator does perform non-zero velocities, resulting in no motion of the tool platform.

However, if the posture is switched, meaning (A) is unfolded and (B) folded, both configurations still correspond to a type 1 singularity, despite the formerly infinite motion—in other words the unrestrained free rotation of the actuator axis—is now reduced to an infinitesimal rotation due to the axes $\hat{\boldsymbol{u}}_j$ and $\hat{\boldsymbol{w}}_j$ not being colinear any more. Hence, any case where the linkages are fully folded or unfolded result in a type 1 singularity, removing one DOF from the manipulator. However, any case where in addition it holds that $\hat{\boldsymbol{u}}_j$ and $\hat{\boldsymbol{w}}_j$ are colinear, unrestrained motion of the actuator axes becomes possible, while still keeping the tool platform at zero velocity. Yet, any such case makes the inverse kinematics solution degenerate.

i: SIMPLIFICATION

Considering the computational effort, (71) can also be implemented in a shorter notation, involving precalculated constant terms. Therefore $\theta_{b,j}$ can be expressed with the constant terms:

$$c_{luv,j} := \cos(l_{uv,j}), \tag{74}$$
$$c_{lvw,j} := \cos(l_{vw,j}), \tag{75}$$
$$s_{luv,j} := \sin(l_{uv,j}), \tag{76}$$

and with the following variables:

$$g_{uw,j} := \cos(\operatorname{acos}(\hat{\boldsymbol{u}}_j \cdot \hat{\boldsymbol{w}}_j)) = \hat{\boldsymbol{u}}_j \cdot \hat{\boldsymbol{w}}_j, \tag{77}$$
$$h_{uw,j} := \sin(\operatorname{acos}(\hat{\boldsymbol{u}}_j \cdot \hat{\boldsymbol{w}}_j)) = \sqrt{1 - g_{uw,j}^2}, \tag{78}$$

which simplifies with the arguments:

$$arg_{nw,j} = \frac{\hat{\boldsymbol{w}}_j \cdot \hat{\boldsymbol{n}}_j}{h_{uw,j}} \tag{79}$$

and:

$$arg_{vw,j} = \frac{c_{lvw,j} - c_{luv,j} \cdot g_{uw,j}}{s_{luv,j} \cdot h_{uw,j}}, \tag{80}$$

to the solution:

$$\theta_{b,j} = \operatorname{acos}\left(arg_{nw,j}\right) f_{flip,un,j} + \operatorname{acos}\left(arg_{vw,j}\right) f_{branch,j} \tag{81}$$

for $arg_{nw,j} \in [-1, +1]$ and $arg_{vw,j} \in [-1, +1]$, which is considered to be the preferred notation in comparison to (71) for implementing the solution of the inverse kinematics on controller hardware. In short, the inverse kinematics solution fails if $g_{uw,j} = 1$, which leads to $h_{uw,j} = 0$, expressing that $\hat{\boldsymbol{u}}_j$ and $\hat{\boldsymbol{w}}_j$ are colinear.

j: SPECIAL CASE REGARDING THE OPTIMAL SPM

In addition to the general solution, using the optimal link angles $l_{vw,j} = \pi/2$ for the distal link and $l_{uv,j} = \pi/2$ for the proximal link, as stated in [38], (81) further simplifies to:

$$\theta_{b,j} = \operatorname{acos}\underbrace{\left(\frac{\hat{\boldsymbol{w}}_j \cdot \hat{\boldsymbol{n}}_j}{h_{uw,j}}\right)}_{arg_{nw,j}} f_{flip,un,j} + \frac{\pi}{2} f_{branch,j} \tag{82}$$

for $arg_{nw,j} \in [-1, +1]$. Also, by defining the reference angle rotated by $\pi/2$ depending on the branch configuration around the actuator axis, the constant offset appearing in (82) can be neglected.

k: WRAPPING OF THE SOLUTION SPACE

With the solution of $\theta_{b,j}$ as presented above, the calculation of $\theta_{l,j}$ and $\theta_{t,j}$ may be approached accordingly, which is shown in the appendix (Sec. C) due its overall similarity.

However, since the result of $\theta_{b,j}$ (from (71), (81), (82)), $\theta_{l,j}$ (from (117)) and $\theta_{t,j}$ (from (124)) is shifted outside of the range $[0, 2\pi]$, a wrapping of the resulting angular position is applied by using the modulo operation as a final step:

$$^{[0,2\pi]}\theta_{b,j} = \theta_{b,j} \bmod 2\pi, \tag{83}$$
$$^{[0,2\pi]}\theta_{l,j} = \theta_{l,j} \bmod 2\pi, \tag{84}$$
$$^{[0,2\pi]}\theta_{t,j} = \theta_{t,j} \bmod 2\pi. \tag{85}$$

3) RESULTS

An example motion of the SPM with its angular positions of all active and passive joints is shown in Fig. 17, which is computed for:

$$^{hf}_{hb}\boldsymbol{R} = \boldsymbol{R}_n(\boldsymbol{n}_t, \alpha_t), \tag{86}$$

with tilt angle $\alpha_t = \pi/6$ and tilt axis $\boldsymbol{n}_t$, where:

$$\boldsymbol{n}_t = \boldsymbol{R}_z(\alpha) \cdot [1, 0, 0]^T, \tag{87}$$

over $\alpha \in [-\pi, +\pi]$. For this example, the SPM features the ideal configuration with arc lengths for proximal and distal links of $\pi/2$, and with angles of $\pi/2$ between neighbouring axes, as shown in [42]. A complete implementation of the geometrical solution is included as MATLAB code in the supplementary materials.

IV. FORWARD KINEMATICS

The forward kinematics for the robot are presented in the following, which deliver the spatial location of the robot end-effectors for a given set of generalized joint coordinates. Thus, considering the vector $\boldsymbol{\theta} \in \mathbb{R}^{12}$ of the actuated joint coordinates known, the evaluation of the forward kinematics of the robot yields the foot position $^{ee}\boldsymbol{p}_i$ for the legs $i = 1, 2, 3$. Regarding the future development of possible robot control strategies, the forward kinematics are an essential component of these control laws, as they are required to reconstruct the current robot posture based on the information from the measurement sensors, which are the encoders

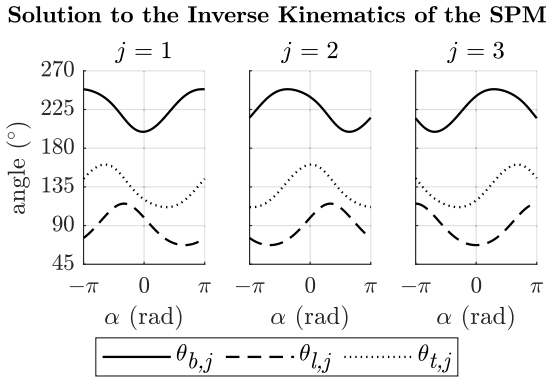

FIGURE 17. Base, link and tool axes angles for an example motion of the SPM, according to (86).

tracking the motion of the motor axes $\hat{\boldsymbol{u}}_j$, support joint axis $\hat{\boldsymbol{c}}_1$, the slider position q_{sl} and spring DOF angle φ_s.

Notably, the foot position vectors ${}^{ee}\boldsymbol{p}_i$ are expressed locally with respect to the torso reference frame $\mathcal{F}_{ee}$, as the global spatial position and orientation of the robot torso in the world reference frame $\mathcal{F}_w$ depends on additional sensor information, which is only applicable with the known measurement matrix ${}^{w}_{ee}\boldsymbol{Q}$ by:

$$ {}^{w}\boldsymbol{p}_i = {}^{w}_{ee}\boldsymbol{Q} \cdot {}^{ee}\boldsymbol{p}_i, \tag{88} $$

and is an important part of future real world controller implementations.

In the following, first the orientation of the hip tool platform is determined by the actuator angles $\theta_{b,1}$, $\theta_{b,2}$, and $\theta_{b,3}$. Thus, with the hip orientation known, the foot position is calculated based on the slider position q_{sl}, which depends on the knee actuator angle θ_4. In addition, the passive DOF due to the leg compliance is included based on a known value for the spring angle φ_s, which is measured through the motion Δx of the spring transmission string.

A. HIP MECHANISM FORWARD KINEMATICS

In the following, the forward kinematics of the SPM is derived by a geometrical approach. Specifically, the calculation of the hip rotation matrix ${}^{hb}_{hf}\boldsymbol{R}$ based on the measured angles $\boldsymbol{\theta}_b$ of the base actuator axes is discussed. Consequently, the orientation of the axes $\hat{\boldsymbol{v}}_j$ is known, as these can be computed as e.g. depicted in (52).

For simplicity, the solution only considers the ideal manipulator configuration with angles of $\pi/2$ between neighbouring axes. Consequently, most of the vector cross products yield vectors that obey to the unit length; however, for the general manipulator, normalizations must be applied.

A reasonable construction of the tool platform orientation may start with vector $\hat{\boldsymbol{w}}_1$, which can be calculated by a rotation with angle α around axis $\hat{\boldsymbol{v}}_1$ of the vector orthogonal to the $\hat{\boldsymbol{u}}_1$-$\hat{\boldsymbol{v}}_1$-plane:

$$ \hat{\boldsymbol{w}}_1 = \boldsymbol{R}_n(\alpha, \hat{\boldsymbol{v}}_1)(\hat{\boldsymbol{v}}_1 \times \hat{\boldsymbol{u}}_1). \tag{89} $$

Thus, under the restriction that the linkages keep their initial assembly configuration, which prevents the linkages from entering singular postures, it must hold the interval $\alpha \in (-\pi/2, +\pi/2)$. Due to the geometry of the ideal manipulator, $\hat{\boldsymbol{w}}_3$ is always orthogonal to $\hat{\boldsymbol{w}}_1$ and $\hat{\boldsymbol{v}}_3$; thus, we can apply:

$$ \hat{\boldsymbol{w}}_3^* = \frac{\hat{\boldsymbol{w}}_1 \times \hat{\boldsymbol{v}}_3}{\left\| \hat{\boldsymbol{w}}_1 \times \hat{\boldsymbol{v}}_3 \right\|} \quad \text{for} \quad \hat{\boldsymbol{w}}_1 \nparallel \pm\hat{\boldsymbol{v}}_3. \tag{90} $$

The non-colinearity of both vectors is essential here, as otherwise the denominator will vanish; yet, this case is mechanically not attainable in general, as this would require to physically align tool and link axes. However, depending on the orientation of the SPM, it may be required to switch the direction of $\hat{\boldsymbol{w}}_3^*$, as the intended configuration of the linkages is not taken into account with (90). Thus, under the assumption that the linkage did not move through a singularity with $\hat{\boldsymbol{u}}_j$ and $\hat{\boldsymbol{w}}_j$ being colinear, we can derive $\hat{\boldsymbol{w}}_3$ by:

$$ \hat{\boldsymbol{w}}_3 = \begin{cases} -\hat{\boldsymbol{w}}_3^* & \text{if } \hat{\boldsymbol{w}}_3 \cdot \hat{\boldsymbol{n}}_3 < 0 \\ \hat{\boldsymbol{w}}_3^* & \text{otherwise,} \end{cases} \tag{91} $$

with the vector $\hat{\boldsymbol{n}}_3$, orthogonal to the $\hat{\boldsymbol{u}}_3$-$\hat{\boldsymbol{v}}_3$-plane, being calculated by:

$$ \hat{\boldsymbol{n}}_3 = \hat{\boldsymbol{v}}_3 \times \hat{\boldsymbol{u}}_3. \tag{92} $$

Finally, as the vectors $\hat{\boldsymbol{w}}_1$, $\hat{\boldsymbol{w}}_2$ and $\hat{\boldsymbol{w}}_3$ represent an orthogonal reference frame, vector $\hat{\boldsymbol{w}}_2$ follows by:

$$ \hat{\boldsymbol{w}}_2 = \hat{\boldsymbol{w}}_1 \times \hat{\boldsymbol{w}}_3. \tag{93} $$

Crucially, as required for the reconstruction of the tool platform orientation, angle α must be obtained. Thus, through the geometry of the linkages, one can deduce that the equation:

$$ f_G(\alpha) = \operatorname{acos}\left(\hat{\boldsymbol{w}}_2(\alpha) \cdot \hat{\boldsymbol{v}}_2\right) - l_{vw} = 0, \tag{94} $$

which is a function of α, must be satisfied for any mechanically valid posture. Consequently, finding the roots of (94) yields α, which then allows to calculate the vectors $\hat{\boldsymbol{w}}_1$, $\hat{\boldsymbol{w}}_2$ and $\hat{\boldsymbol{w}}_3$ via (89)–(93). Importantly, due to the mechanical restriction to allow for only one assembly mode, which is a reasonable assumption regarding the mechanical realization of the manipulator, (94) represents a first order root finding problem, which allows for a simple numerical calculation, e.g. by a bisection method.

Once the axes $\hat{\boldsymbol{w}}_1$, $\hat{\boldsymbol{w}}_2$ and $\hat{\boldsymbol{w}}_3$ are determined, the orientation matrix ${}^{hb}_{hf}\boldsymbol{R}$ can be constructed for the further calculation of the robot forward kinematics. Thus, it follows:

$$ {}^{hb}_{hf}\boldsymbol{R} = \left[{}^{hb}\hat{\boldsymbol{w}}_1, {}^{hb}\hat{\boldsymbol{w}}_2, {}^{hb}\hat{\boldsymbol{w}}_3 \right] \cdot \left[{}^{hb}\hat{\boldsymbol{w}}_1^*, {}^{hb}\hat{\boldsymbol{w}}_2^*, {}^{hb}\hat{\boldsymbol{w}}_3^* \right]^T, \tag{95} $$

while * denotes the home configuration of the tool platform vectors $\hat{\boldsymbol{w}}_j$, expressed in the hip base reference system $\mathcal{F}_{hb}$, which are known for ${}^{hb}_{hf}\boldsymbol{R} = \boldsymbol{I}$ with identity matrix $\boldsymbol{I}$.

B. LEG PLANE FORWARD KINEMATICS

The forward kinematics of the leg plane is solved by first calculating the length of the upper leg l_0, which constitutes to:

$$l_0 = \sqrt{a_5^2 + (a_6 + q_{sl})^2}, \tag{96}$$

with the slider position q_{sl} given by:

$$q_{sl} = \frac{p}{2\pi}(\theta_4 - \alpha_z). \tag{97}$$

However, the sensor in the actual robot model measures the position of the slider q_{sl} directly, which—in consequence—does not strictly require the evaluation of (97).

The knee angle α_1 follows with:

$$\alpha_1 = 2\pi - \lambda_6 - \lambda_5 - \delta_3, \tag{98}$$

with λ_5 and λ_6 being defined by:

$$\lambda_5 = \operatorname{acos}\left((a_4^2 + b_2^2 - a_2^2) \cdot (2\, a_4\, b_2)^{-1}\right), \tag{99}$$

$$\lambda_6 = \operatorname{acos}\left((l_0^2 + b_2^2 - a_1^2) \cdot (2\, l_0\, b_2)^{-1}\right). \tag{100}$$

Side length b_2 as required above is calculated by:

$$b_2 = \sqrt{l_0^2 + a_1^2 - 2\, l_0 a_1 \cos(\lambda_7 + \lambda_8)}. \tag{101}$$

C. COMBINED SPATIAL FORWARD KINEMATICS

Finally, the foot position follows through the combination of the planar leg geometry and the spherical hip mechanism. With respect to the y-z-plane of the hip follower frame, it holds:

$${}^{hf}\boldsymbol{p} = \begin{bmatrix} 0 \\ -l_0 \sin(\alpha_p) - l_1 \sin(\alpha_p + \alpha_d) \\ +l_0 \cos(\alpha_p) + l_1 \cos(\alpha_p + \alpha_d) \end{bmatrix}, \tag{102}$$

where the proximal and distal angles are:

$$\alpha_p = \lambda_7 - \varphi_s \quad \text{and} \quad \alpha_d = \pi - \alpha_1. \tag{103}$$

Thus, the foot position ${}^{w}\boldsymbol{p}$ of leg i is evaluated by:

$${}^{w}\boldsymbol{p}_i = {}^{w}_{ee}\boldsymbol{Q} \cdot {}^{ee}_{hb}\boldsymbol{Q}_i \cdot \begin{bmatrix} {}^{hb}_{hf}\boldsymbol{R}_i \cdot [0, {}^{hf}p_{y,i}, {}^{hf}p_{z,i}]^T \\ 1 \end{bmatrix}. \tag{104}$$

In this regard, (102) resembles a classical 2-link planar manipulator, which is rotated in the $\mathbb{R}^3$ in (104) and mapped into the torso reference frame $\mathcal{F}_{ee}$ space.

V. ROBOT MOTION KINEMATICS

Fig. 18 depicts multiple postures A–I of a motion sequence, captured from the simulation framework written in C++/OpenGL for the robot project. The framework gathers its data from a Simulink model that runs the robot controller compiled into a standalone application due to the increased execution speed. The interprocess data communication is realized via a TCP/IP connection. This data is then visualized, depicting the motion of the robot, which may either be the result of a pure kinematics or a more sophisticated multi-body dynamics simulation. A video of the sequence is included in the supplementary materials. The trajectory over time is shown in the Fig. 23 in the appendix.

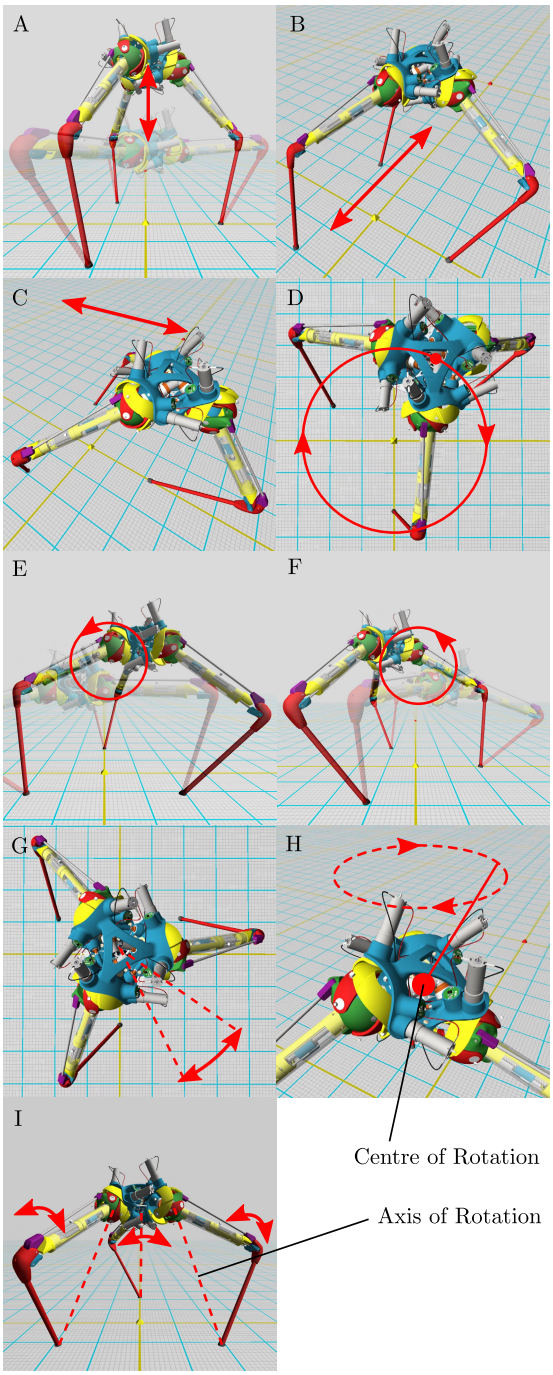

FIGURE 18. States A–I of the robot kinematics motion. A video is included in the supplementary materials. A–C are translational in one direction. D–F translate in two directions and create circular motions. G–H rotate the body. I shows functionally redundant motion.

Thus, for a given target posture, which includes position and orientation of the robot torso, and the target positions for the feet, the implementation of the inverse kinematics presented in the previous sections delivers the joint coordinates necessary. Afterwards, these coordinates are measured

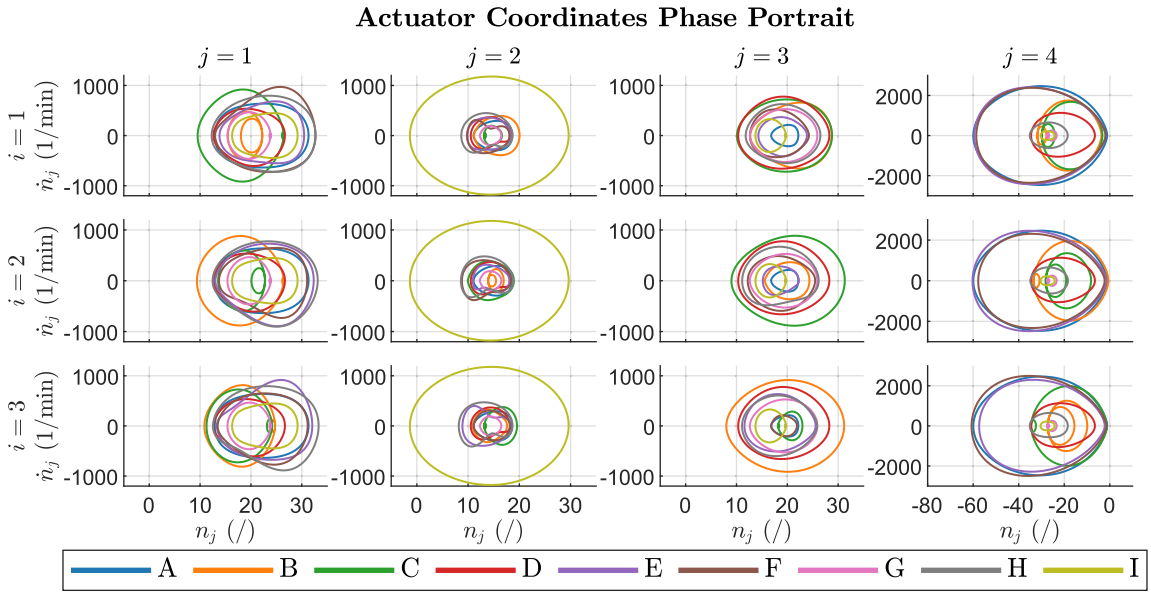

FIGURE 19. Phase portraits of the motor units for the motion sequences depicted in Fig. 18. The diagrams depict the velocity of the motor axes expressed over the number of rotations of the respective axes. Values correspond to the motor axes behind the gear heads.

virtually and used to compute the forward kinematics, which fully reconstructs the robot posture. From this posture, each joint transformation matrix connecting individual bodies can be extracted, which is then used for the forward homogeneous matrix calculations of the robot. This calculation then determines the spatial position and orientation of each body part of the robot, and is visualized in the 3D rendering, as shown in the figure. Consequently, Fig. 24 in the appendix shows the corresponding joint coordinates over time.

A. RESULTS

An important consideration stemming from the robot motion must be placed upon the requirements for the actuators regarding their position and velocity profiles. As each actuator used in the robot entails the identical motor unit, it is reasonable to consider the respective gear heads as part of the kinematics model. Consequently, the position and velocities will be amplified towards the internal motor axis by the gear head ratios $r_B = 150:1$ and $r_K = 35:1$ for the base and knee actuators. Based on the performed motion sequence, the resulting phase portraits are shown in Fig. 19 for all 12 DC-motors.

Interestingly, the phase portraits for the motors j = 1 and j = 3 show similar utilization, which are the motor units placed close to the lower side of the robot torso. On the contrary, unit j = 2 shows noticeably less utilization during normal motion; however, this axis becomes highly active at sequence I, which depicts the functionally redundant leg tilt motion.

Similarly, the knee motor unit shows a generally small motion at the sequences (B, C, D, G, H, I). The remaining sequences (A, E, F) however show significant utilization,

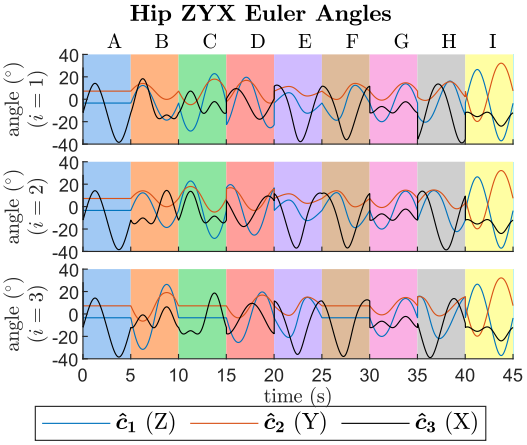

FIGURE 20. Angles around the axes $\hat{c}_1$, $\hat{c}_2$ and $\hat{c}_3$ of the internal RRR joint structure for each leg $i = 1, 2, 3$. The angles are derived by the ZYX-Euler decomposition of the hip rotation matrix.

which is due to (A, E, F) being motions that are highly variable regarding the height of the torso. This naturally results in a more pronounced application of the knee joint. Hence, any vertical motion of the torso applies a noticeably higher demand on the knee motor unit than horizontal motions in general.

Crucially, the motion profiles are not exceeding the respective joint range limitations of $[-40°, +40°]$ for the RRR joint axes that are located in the hip centres, which is an important result as it shows that the mechanical design is not compromised by internal collisions. Fig. 20 shows the angles along the axes $\hat{c}_1, \hat{c}_2$ and $\hat{c}_3$, while a value of zero for all axes corresponds to the isotropic configuration with ${}^{hb}_{hf}\boldsymbol{R} = \boldsymbol{I}$.

VI. DISCUSSION

In the following, certain points of interest will be discussed, based on the results of the inverse and forward kinematics of the three-legged robot presented.

A. GENERAL ROBOT KINEMATICS

With the solution to the robot kinematics being implemented in software, the results of the motion simulation from Sec. V show that the robot is kinematically able to adapt to many different postures. Especially, the analysis reveals that the motor phase profiles work in similar conditions, with the exception of the more pronounced utilization of the knee motor for vertical motions and the lesser demand on motor $j = 2$, except for redundant motions. Thereby, the analysis shows resulting motor profiles that realistically can be achieved by the employed hardware. This, in general, reveals a high potential for the robot to be applicable for both manipulation tasks and possibly legged locomotion. However, the resulting performance will certainly depend on the control algorithm employed and the physical capabilities of actuator and sensor hardware.

Crucially, the top-down approach by dividing the kinematics into sub-problems, starting from a simplified substitute model as shown in Sec. II-B and III-A down to suitably more complex low level kinematics problems yields a complete, yet readable solution for the legged robot. This approach allows the robot to be considered as a general 3-SR type mechanism with 4-DOF legs, allowing for a wide range of motions and for simple high-level kinematics, referring to Sec. III-A1. In this regard, given the functional redundancy due to its leg tilting capability, as examined in Sec. III-A2, without altering its feet positions, the robot additionally allows for the optimisation of the actuator load distribution and improved conditioning.

As required for the combination of both leg dexterity and elastic compressibility, a closed-loop mechanism was included into the leg system. Still, despite the complex design, the kinematics analysis from Sec. III-B1 shows that the legs are able to expand and retract over a reasonable distance, important to allow for a suitable workspace. In addition, as revealed in Sec. III-B2, the leg compression will influence the position of the feet only to a minor degree, as they stay close to the virtual line between initial and hip centre point. Hence, with the lateral disturbance kept small, only minor adjustments to the joint coordinates may be required for an accurate alignment of actual and desired feet positions. Additionally, the motion performance shows that despite the utilization of the complex hip structure, the mechanism does not reach postures that are critically close to singular configurations. Similarly, the employment of the internal universal support structure still allows for a reasonable workspace of the hip manipulator, despite being the limiting factor of the attainable maximum range of the spherical mechanism structure. Crucially, this structure allows the specific placement of the knee actuator, kinematically connected to the leg, as depicted in Sec. III-B3. In this regard, it is shown by the results of Sec. III-B4 that the possible disturbances by the spherical motion of the hip joint can be counteracted by the kinematic relationship between knee actuator and upper leg. Fundamentally, the kinematic design of the robot realizes the design goals of the robot, initially stated in Sec. I-A.

B. HIP MANIPULATOR KINEMATICS

Regarding the derived SPM inverse kinematics, the geometric approach presented in this proposal leads to only one solution with an explicit result of three angles, one for each actuator axis. This is in contrast e.g. to the often adopted approach shown in [42], [43], leading to eight solutions in total. Similarly, in contrast to the approach shown in [41], again yielding eight possible solutions, the forward kinematics solution presented returns just one orientation of the tool platform. Thus, based on a known initial layout of the manipulator, for both the inverse and forward case it does not exist any confusion, which of the returned results is the mechanically applicable one.

Fundamentally, this result stems from the initial restrictions applied in the derivation of the geometric solution for both the inverse and forward kinematics, predetermining the general posture of the manipulator to some degree. Consequently, this simplifies the mathematical expressions noticeably, and might even reduce the runtime of its real world implementations. Additionally, due to the lower number of mathematical operations, this may increase the numerical accuracy of the returned solutions. However, an in-depth analysis regarding runtime and accuracy is outside of the scope of this article.

Still, as a general remark, using the solution presented in an actual implementation requires to specifically select the configuration of the physical manipulator, which then must be kept in its intended working and assembly mode throughout its application. However, typically only one of the mathematically thinkable solutions is mechanically intended or even feasible, regarding possible internal collisions between parts.

C. MODES AND SINGULARITIES

Since singularities alter the behaviour of the mechanism significantly and yield manipulators to gain or lose DOFs, special attention must be provided to those configurations. In addition, postures near those states represent configurations with a highly unequal input-output-relationship of the manipulator, regarding velocities and torques, respectively. However, this might be exploited as a property, allowing the manipulator to resist torques from specific directions, yet makes it highly sensitive to torques from other directions. Alternatively, yet correspondingly, high precision due to a very small output velocity in contrast to a high input velocity might be considered, which then may be affected by an inaccurate motion in some other direction. For reference, the specific utilization of the SPM as a hip joint for the purpose of locomotion might improve with a specifically designed

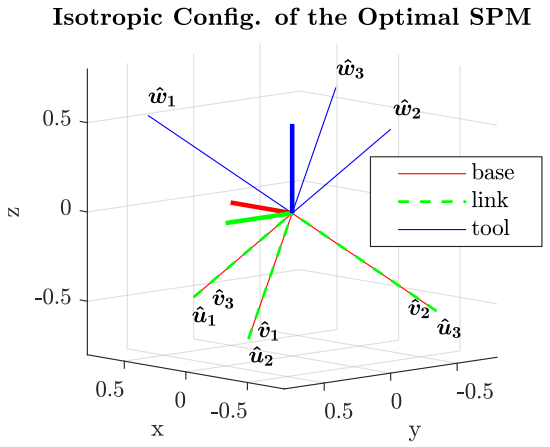

FIGURE 21. Posture of the optimal SPM in the isotropic home configuration. Axes correspond to the values listed in Table 3.

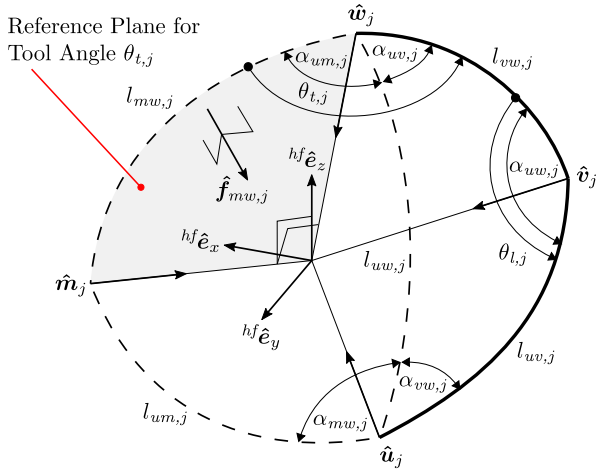

FIGURE 22. Geometry for the calculation of the remaining passive joint angles inside the SPM.

TABLE 4. Table of symbols, parameters and abbreviations.

Symbol	Description
SPM	Spherical Parallel Manipulator
DOF	Degree of Freedom
EE	End-effector
CAD	Computer Aided Design
$\mathcal{F}$	General orthogonal reference frame
$\mathcal{F}_w$, $\mathcal{F}_{ee}$	World/end-effector (torso) reference frame
$\mathcal{F}_{hb}$, $\mathcal{F}_{hf}$	Hip base/follower reference frame
$\mathcal{F}_{kb}$, $\mathcal{F}_{kf}$	Knee base/follower reference frame
$\boldsymbol{R}$	Matrix of SO(3) applying a rotation
$\boldsymbol{Q}$	Matrix applying an affine transformation
i	Index denoting leg 1, 2 or 3
j	Index denoting a linkage chain 1, 2 or 3
$\hat{\boldsymbol{u}}_j$	SPM base actuator axis j
$\hat{\boldsymbol{v}}_j$	SPM link axis j
$\hat{\boldsymbol{w}}_j$	SPM tool axis j
$\hat{\boldsymbol{c}}_k$	Joint axis of rotation with index k
$\hat{\boldsymbol{u}}_4$	Knee actuator axis
$\boldsymbol{p}_i$	Spatial position of the robot foot of leg i
$\theta_{b,j}$	Base actuator joint coordinate of linkage j
$\theta_{l,j}$	Link joint coordinate of linkage j
$\theta_{t,j}$	Tool joint coordinate of linkage j
θ_4, θ_k	Knee actuator joint coordinate
$\boldsymbol{\theta}_b$	Vector equal to $[\theta_{b,1}, \theta_{b,2}, \theta_{b,3}]$
$\boldsymbol{\theta}_l$	Vector equal to $[\theta_{l,1}, \theta_{l,2}, \theta_{l,3}]$
$\boldsymbol{\theta}_t$	Vector equal to $[\theta_{t,1}, \theta_{t,2}, \theta_{t,3}]$
$\boldsymbol{\theta}_i$	Vector equal to the active joint coordinates $[\boldsymbol{\theta}_{b,i}, \theta_{4,i}]$ of leg i
$\boldsymbol{\theta}$	Vector of all 12 DC actuator joint coordinates, equal to $[\boldsymbol{\theta}_1, \boldsymbol{\theta}_2, \boldsymbol{\theta}_3]$
η	Leg tilt angle
l_0, l_1	Length of upper and lower leg
d	Distance between hip centre and foot tip
a_k	Static length k
b_k	Variable length k
q_{sl}	Slider position
p	Pitch of the lead screw
φ_s	Spring slot angle
$\varphi_{s,min}$	Spring slot lower angle limit
$\varphi_{s,max}$	Spring slot upper angle limit

configuration in future works, possibly prioritizing torque over accuracy, yet in this work, we settle on the known optimal design of the SPM.

Importantly, as initially expressed with (61) and shown by the aforementioned discontinuities, there is the risk that the linkages might flip their initial branch configuration after passing a singularity, resulting in a misaligned and unrecoverable mechanical posture. More specifically, crossing a singularity means that the manipulator switches its working and assembly mode [13], [17]. However, since each unique solution to the inverse and forward kinematics problem corresponds to one mode, transitioning to a different mode makes the solution to the kinematics problem invalid—if not properly detected—possibly and mechanically damaging the manipulator due to the invalid control signals, imposing a safety concern. However, as the robot comprises mechanical limitations in the leg plane and due to the universal joint structure, the legs cannot enter these singular postures.

D. VISUAL REPRESENTATION

Notably, the solutions for the inverse and forward kinematics problem of the SPM presented in this article is considered by the author of this work to be an equally valid alternative to [43] and [42], because fundamentally, it solves the same problem. However, the representation of the solution presented in this article offers the possibility for a certainly direct implementation and convenient usage in software applications. Furthermore, due to the geometric approach, the solution offers a direct insight into the kinematical behaviour of the mechanism, since its terms allow for an easy visual representation.

Essentially, due to the expressive meaning of the terms, e.g. the degeneration of the inverse kinematics at type 1 singularities with colinear axes becomes obvious by just observing the equation. In addition, the visual representation of the base axes zero-position—visualized by the definition of the reference planes—offers a clear geometrical meaning regarding the initial angle of the actuator position. Similarly,

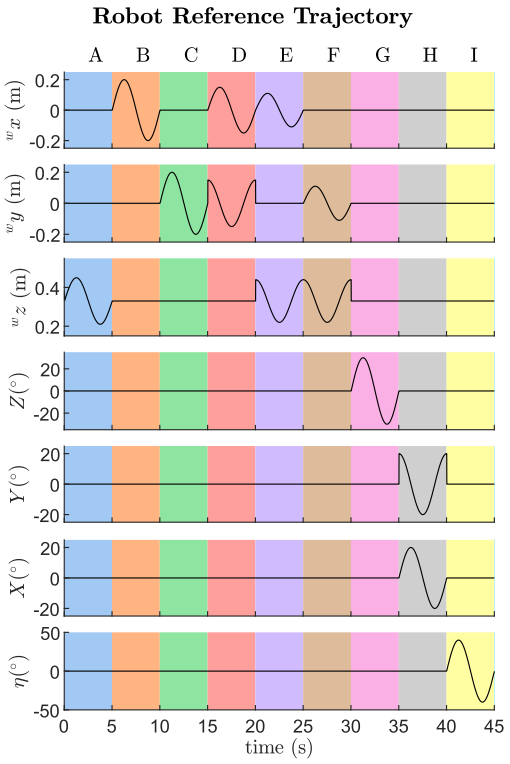

FIGURE 23. Reference trajectory A–I of the robot torso. $^w x$, $^w y$ and $^w z$ represent the position of the torso in the world reference frame $\mathcal{F}_w$. Angles X, Y and Z express the torso orientation, derived from the ZYX-Euler decomposition.

the forward kinematics problem becomes an intuitively digestible vector construction, as there is no need for lengthy polynomial equations. Lastly, the geometric approach can be applied equally to calculate the remaining angles of the linkage structure, as shown in Sec. III, which thus yields a complete solution for all joint angles of the SPM.

E. MEASUREMENT REDUNDANCY

Fundamentally, real world mechanisms are affected by manufacturing errors and measurement inaccuracies. Thus, a prototype robot will be limited to a certain rigidity and accuracy of its parts, with the sensory hardware physically limited to a certain measurement resolution.

In this regard, as one can observe in Fig. 2, the base axis of the support structure is equipped with an additional rotatory encoder, which thus is able to track the effect on spherical rotations of the SPM on axis $\hat{\boldsymbol{c}}_1$. Consequently, this additional information may improve the accuracy of the forward kinematics solution, as it is partially redundant to the three base encoders of the axes $\hat{\boldsymbol{u}}_1$, $\hat{\boldsymbol{u}}_2$ and $\hat{\boldsymbol{u}}_3$.

However, the inclusion of this fourth and redundant encoder may require a different set of equations or even a fundamentally different approach to express the kinematics relationships, which—due to its redundant nature—will yield a mathematically overdetermined system. In this regard, the knowledge of all joint angles for a certain orientation of the tool platform, as delivered by the inverse kinematics solution, might actually be of practical importance. Specifically, measuring the joint axes redundantly possibly yields to an optimisation problem. Thus, with the complete set of all joint angles for any target orientation, this set of joint coordinates might be employed as an initial guess for the potential application of optimization strategies as a measure to identify the actual posture of the robot despite the non-ideal circumstances of real world applications. Consequently, a possible optimization algorithm may converge to an optimum with less iterations, based on the guessed manipulator posture, constructed from the full set of active and passive joint coordinates. However, the specific consequences of the redundant measurement set-up and its solution need to be investigated in future works.

VII. CONCLUSION

In this article, the inverse and forward kinematics for a mechanically complex, serial-parallel, redundant, compliant three-legged robot was presented by utilising a top-down approach through a simplified substitute model. This solution is fundamentally required for the further implementation in control algorithms, which either require the joint state for a desired robot posture, or the reconstruction of a posture based on measured joint angles.

As a major component—regarding the spherical parallel manipulator utilised for the robot hip mechanism—the inverse kinematics of this structure was solved via spherical trigonometry, and the forward kinematics via spatial vector geometry. In addition, the solution to the inverse kinematics was extended to all nine joints of the general spherical parallel manipulator.

Interestingly, and generally speaking, this geometrical approach to the solution of the inverse and forward kinematics reduces the complexity of the solution due to the implicit reduction of the variety of the manipulator working and assembly modes to only a single mode, yielding a unique solution for both the inverse and forward case. In practice, this is reasonable, as switching modes requires the mechanism to cross singularities, which is not advisable as this steers the manipulator into unstable and functionally undesirable states. Fundamentally, this allows the derived solutions to represent simple and visually expressive alternatives to the literature standard solutions for the spherical parallel manipulator.

Finally, the resulting solution to the robot kinematics was implemented in software and verified via a simulation model, showing the robot performing several motion sequences. Based on the analysis of the actuator phase portraits, it was found that the utilisation is generally well distributed over the different motor units and that the resulting position-velocity-profiles lie within ranges reasonable for the selected real-world actuators. The results furthermore revealed the correlation between specific motor units and the redundant tilting motion of the leg, with one unit per leg becoming highly active.

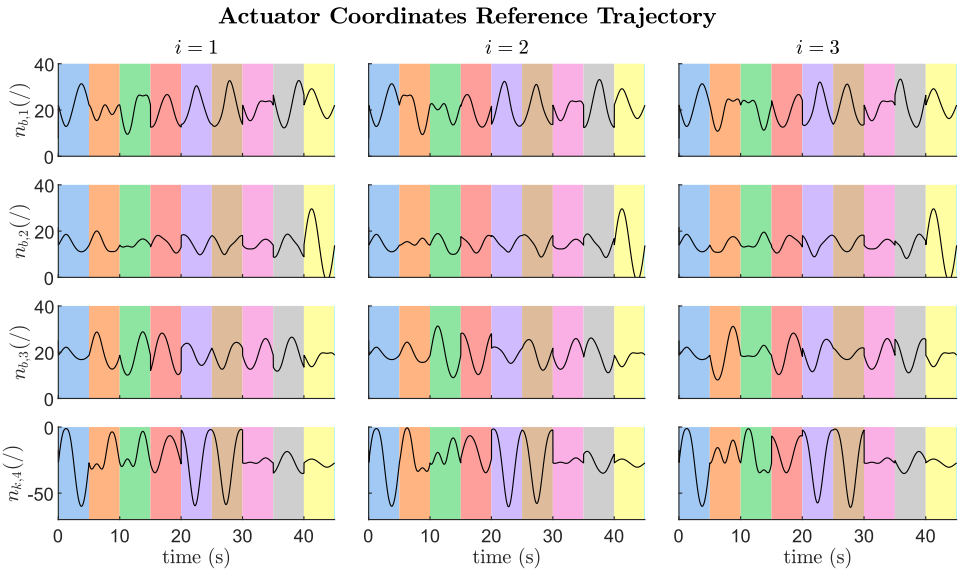

FIGURE 24. Joint coordinates of the actuator axes corresponding to the robot reference trajectory A–I from Fig. 23. Value *n* expresses the number of rotations of the motor axes behind the actuator gear heads.

Crucially, this simulation shows the general mobility of the robot, which can adapt to many postures, and—due to its functional redundancy—allows for posture optimisations with regard to possibly increased manipulator accuracy, benefiting its application for manipulation tasks. Eventually, in future works, the torso centric mass and the leg compliance may possibly allow for agile legged locomotion.

SUPPLEMENTARY MATERIAL

- MATLAB example function implementing the discussed axes construction methods for the SPM from Sec. III-C2.c and Sec. III-C2.d: File `MAIN_ExampleImpl.m` in folder `SPM_InvKineAllJoints`.
- Implementation of the derived geometrical solution to the inverse kinematics of the general SPM for all active and passive joints from Sec. III as MATLAB function: Files `SPM_InvKineJointsMain.m` and `SPM_InvKineJointsRest.m` in folder `SPM_InvKineAllJoints`.
- Video of the kinematics simulation, performing the motion profiles A–I.

APPENDIX. EXTENDED INFORMATION

In this section, equations are collected that are not relevant for the readers' understanding, yet capture additional geometrical relationships of the mechanism. As these equations are implemented in the corresponding MATLAB functions, they are provided with this article.

A. LEG TRIGONOMETRICAL EQUATIONS

The following equations depict the geometrical relationships of the planar leg mechanism, as referred to in Sec. III-B:

$$l_1^2 + a_4^2 - a_3^2 = 2 \cdot l_1 \cdot a_4 \cdot \cos(\delta_3). \tag{105}$$

$$a_4^2 + b_1^2 - l_0^2 = 2 \cdot a_4 \cdot b_1 \cdot \cos(\lambda_4), \tag{106}$$

$$a_4^2 + b_2^2 - a_2^2 = 2 \cdot a_4 \cdot b_2 \cdot \cos(\lambda_5), \tag{107}$$

$$b_2^2 + l_0^2 - a_1^2 = 2 \cdot b_2 \cdot l_0 \cdot \cos(\lambda_6), \tag{108}$$

$$b_2^2 + a_1^2 - l_0^2 = 2 \cdot b_2 \cdot a_1 \cdot \cos(\lambda_1), \tag{109}$$

$$a_2^2 + b_2^2 - a_4^2 = 2 \cdot a_2 \cdot b_2 \cdot \cos(\lambda_2), \tag{110}$$

$$b_1^2 + a_2^2 - a_1^2 = 2 \cdot b_1 \cdot a_2 \cdot \cos(\lambda_3), \tag{111}$$

$$l_0^2 + b_1^2 - a_4^2 = 2 \cdot l_0 \cdot b_1 \cdot \cos(\lambda_9), \tag{112}$$

$$b_1^2 + a_1^2 - a_2^2 = 2 \cdot b_1 \cdot a_1 \cdot \cos(\lambda_{10}). \tag{113}$$

In addition, the combination of neighbouring angles holds true:

$$l_0^2 + a_1^2 - b_2^2 = 2 \cdot l_0 \cdot a_1 \cdot \cos(\lambda_7 + \lambda_8), \tag{114}$$

$$a_4^2 + l_0^2 - b_1^2 = 2 \cdot a_4 \cdot l_0 \cdot \cos(\lambda_5 + \lambda_6). \tag{115}$$

B. ISOTROPIC CONFIGURATION

The isotropic configuration of the SPM is depicted in Fig. 21.

C. COMPUTATION OF THE REMAINING SPM ANGLES

Considering the whole solution of the inverse kinematics as a problem of spherical trigonometry, referring back to Sec. III-C, the remaining angles of the linkage structure of the SPM can be computed easily. Calculating these angles may be important for a real application, since mechanical restrictions can limit the actual workspace of the manipulator, leading to joint boundaries limiting the possible range of these angles that have to be considered, despite of having computed a valid solution for the actuator angles alone. Therefore, according to

Fig. 22, the link angles $\theta_{l,j}$ are derived with:

$$\alpha_{uw,j} = \text{acos}\underbrace{\left(\frac{\text{cos}l_{uw,j} - \text{cos}l_{vw,j} \cdot \text{cos}l_{uv,j}}{\text{sin}l_{vw,j} \cdot \text{sin}l_{uv,j}}\right)}_{arg_{uw,j}} \tag{116}$$

for $arg_{uw,j} \in [-1, +1]$ to:

$$\theta_{l,j} = \alpha_{uw,j} \cdot f_{branch,j}. \tag{117}$$

To solve the angle between a fixed reference orientation of the tool platform and the proximal link, an analog geometrical approach can be made, see Fig. 15 and Fig. 22. Here, a reference vector ${}^{hf}\hat{\boldsymbol{m}}_j$, fixed to the tool platform is constructed:

$${}^{hf}\hat{\boldsymbol{m}}_j = \frac{{}^{hf}\hat{\boldsymbol{w}}_j \times {}^{hf}\hat{\boldsymbol{e}}_z}{\|{}^{hf}\hat{\boldsymbol{w}}_j \times {}^{hf}\hat{\boldsymbol{e}}_z\|}, \tag{118}$$

and mapped into the base reference frame $\mathcal{F}_{hb}$ of the hip joint:

$${}^{hb}\hat{\boldsymbol{m}}_j = {}^{hb}_{hf}\boldsymbol{R} \cdot {}^{hf}\hat{\boldsymbol{m}}_j \tag{119}$$

with the normal vector of the tool platform reference plane:

$$\hat{\boldsymbol{f}}_{mw,j} = -{}^{hb}\hat{\boldsymbol{m}}_j \times {}^{hb}\hat{\boldsymbol{w}}_j, \tag{120}$$

which is accounted for in the flip factor for the tool reference plane:

$$f_{flip,mw,j} := \begin{cases} +1 & \text{for} \hat{\boldsymbol{f}}_{mw,j} \cdot {}^{hb}\hat{\boldsymbol{u}}_i < 0 \\ -1 & \text{for} \hat{\boldsymbol{f}}_{mw,j} \cdot {}^{hb}\hat{\boldsymbol{u}}_i \geq 0. \end{cases} \tag{121}$$

Again, two spherical triangles are applied to the cosine rule, which leads to:

$$\alpha_{uv,j} = \text{acos}\underbrace{\left(\frac{\text{cos}l_{uv,j} - \text{cos}l_{vw,j} \cdot \text{cos}l_{uw,j}}{\text{sin}l_{vw,j} \cdot \text{sin}l_{uw,j}}\right)}_{arg_{uv,j}}, \tag{122}$$

$$\alpha_{um,j} = \text{acos}\underbrace{\left(\frac{\text{cos}l_{um,j} - \text{cos}l_{mw,j} \cdot \text{cos}l_{uw,j}}{\text{sin}l_{mw,j} \cdot \text{sin}l_{uw,j}}\right)}_{arg_{um,j}}, \tag{123}$$

for $arg_{um,j} \in [-1, +1]$ and $arg_{uv,j} \in [-1, +1]$, which delivers the angle $\theta_{t,j}$ by:

$$\theta_{t,j} = \alpha_{um,j} \cdot f_{flip,mw,j} + \alpha_{uv,j} \cdot f_{branch,j}. \tag{124}$$

D. TABLE OF SYMBOLS

Table 4 shows a list of symbols used throughout this article.

E. MOTION TRAJECTORIES

The joint and task space trajectories of the motion profiles A–I are depicted in the figures 23 and 24.

REFERENCES

[1] Marm. *The New Three-Leg Robot to Transport Weights and Manipulate Components in Space*. Accessed: Aug. 10, 2020. [Online]. Available: https://opentalk.iit.it/en/marm-the-new-three-leg-robot-to-transport-weights-and-manipulate-components-in-space/
[2] S. Aksungur, M. Aydin, and O. Yakut, "Real-time PID control of a novel RCM mechanism designed and manufactured for use in laparoscopic surgery," *Ind. Robot: Int. J. Robot. Res. Appl.*, vol. 47, no. 2, pp. 153–166, Nov. 2019.
[3] K. Al-Widyan, X. Q. Ma, and J. Angeles, "The robust design of parallel spherical robots," *Mechanism Mach. Theory*, vol. 46, no. 3, pp. 335–343, 2011.
[4] R. I. Alizade, N. R. Tagiyev, and J. Duffy, "A forward and reverse displacement analysis of an in-parallel spherical manipulator," *Mechanism Mach. Theory*, vol. 29, no. 1, pp. 125–137, Jan. 1994.
[5] S. Bai and J. Angeles, "A unified input–output analysis of four-bar linkages," *Mechanism Mach. Theory*, vol. 43, no. 2, pp. 240–251, Feb. 2008.
[6] S. Bai, M. R. Hansen, and T. O. Andersen, "Modelling of a special class of spherical parallel manipulators with Euler parameters," *Robotica*, vol. 27, no. 2, pp. 161–170, Mar. 2009.
[7] S. Bai and M. R. Hansen, "Forward kinematics of spherical parallel manipulators with revolute joints," in *Proc. IEEE/ASME Int. Conf. Adv. Intell. Mechatronics*, Jul. 2008, pp. 522–527.
[8] S. Bai, M. R. Hansen, and J. Angeles, "A robust forward-displacement analysis of spherical parallel robots," *Mechanism Mach. Theory*, vol. 44, no. 12, pp. 2204–2216, Dec. 2009.
[9] S. Bai, X. Li, and J. Angeles, "A review of spherical motion generation using either spherical parallel manipulators or spherical motors," *Mechanism Mach. Theory*, vol. 140, pp. 377–388, Oct. 2019.
[10] J. Baumgärtner, E. Badreddin, L. Masia, F. Stolzenberger, M. Goebels, S. Ducati, and S. Otto. *Triped, Non-Mimetic Walking System for Research on Novel Locomotion Methods*. Accessed: May 20, 2023. [Online]. Available: https://triped-robot.github.io/ and https://www.imt.uni-stuttgart.de/en/research/research-projects/triped/
[11] R. Blickhan, "The spring-mass model for running and hopping," *J. Biomechanics*, vol. 22, nos. 11–12, pp. 1217–1227, Jan. 1989.
[12] C. Bombin, L. Ros, and F. Thomas, "On the computation of the direct kinematics of parallel spherical mechanisms using Bernstein polynomials," in *Proc. IEEE Int. Conf. Robot. Autom.*, vol. 4, 2001, pp. 3332–3337.
[13] I. A. Bonev, D. Chablat, and P. Wenger, "Working and assembly modes of the agile eye," in *Proc. IEEE Int. Conf. Robot. Autom.*, Jul. 2006, pp. 2317–2322.
[14] S. Cai, J. Lei, and J. Rao, "Configuration design and load capacity analysis of pelvic fracture reduction robot," *J. Vibroengineering*, vol. 25, no. 5, pp. 996–1010, Aug. 2023.
[15] E. Celaya, *Interval Propagation for Solving Parallel Spherical Mechanisms*. Dordrecht, The Netherlands: Springer, 2002, pp. 415–422.
[16] J. J. Cervantes-Sánchez and H. I. Medellín-Castillo, "A robust classification scheme for spherical 4R linkages," *Mechanism Mach. Theory*, vol. 37, no. 10, pp. 1145–1163, Oct. 2002.
[17] D. Chablat and P. Wenger, "Working modes and aspects in fully parallel manipulators," in *Proc. IEEE Int. Conf. Robot. Autom.*, vol. 3, Dec. 1998, pp. 1964–1969.
[18] A. Chaker, A. Mlika, M. A. Laribi, L. Romdhane, and S. Zeghloul, "Synthesis of spherical parallel manipulator for dexterous medical task," *Frontiers Mech. Eng.*, vol. 7, no. 2, pp. 150–162, Jun. 2012.
[19] A. Chaker, A. Mlika, M. A. Laribi, L. Romdhane, and S. Zeghloul, "On the kinematics of spherical parallel manipulators for real time applications," in *Design and Modeling of Mechanical Systems*, M. Haddar, L. Romdhane, J. Louati, A. B. Amara, Eds. Berlin, Germany: Springer, 2013, pp. 53–60.
[20] Z. Chebili, S. Alem, and S. Djeffal, "Comparative analysis of stiffness in redundant co-axial spherical parallel manipulator using matrix structural analysis and VJM method," *Iranian J. Sci. Technol., Trans. Mech. Eng.*, Apr. 2023, doi: 10.1007/s40997-023-00635-z.
[21] Y. J. Chen, W.-C. Tung, W.-R. Lee, B. Patel, V. Bučinskas, M. Greitans, and P. T. Lin, "Designing and controlling a self-balancing platform mechanism based on 3-RCC spherical parallel manipulator," *Robotic Syst. Appl.*, vol. 3, no. 1, pp. 1–16, Mar. 2023.
[22] Z. Chen, X. Chen, M. Gao, C. Zhao, K. Zhao, and Y. Li, "Motion characteristics analysis of a novel spherical two-degree-of-freedom parallel mechanism," *Chin. J. Mech. Eng.*, vol. 35, no. 1, p. 29, Apr. 2022.

[23] A. T. Cruz-Reyes, M. Arias-Montiel, and R. Tapia-Herrera, "Kinematic analysis of a coaxial 3-RRR spherical parallel manipulator based on screw theory," in *Mechanism Design for Robotics*, S. Zeghloul, M. A. Laribi, and M. Arsicault, Eds. Cham, Switzerland: Springer, 2021, pp. 28–37.

[24] H. Cui, W. Yang, Q. Li, Y. Yu, L. Ma, and Y. Wang, "A new design of three-legged robot of mechanical and control system," in *Proc. 2nd Int. Symp. Comput., Commun., Control Automat. (ISCCCA)*. Atlantis Press, Feb. 2013, pp. 508–511, doi: 10.2991/isccca.2013.126.

[25] A. Degirmenci, F. L. Hammond, J. B. Gafford, C. J. Walsh, R. J. Wood, and R. D. Howe, "Design and control of a parallel linkage wrist for robotic microsurgery," in *Proc. IEEE/RSJ Int. Conf. Intell. Robots Syst. (IROS)*, Sep. 2015, pp. 222–228.

[26] J. L. dos Santos and C. L. Nascimento, "Gait synthesis for a three-legged robot using learning automata," in *Proc. 15th Int. Conf. Adv. Robot. (ICAR)*, Jun. 2011, pp. 271–276.

[27] Y. Du, R. Li, D. Li, and S. Bai, "An ankle rehabilitation robot based on 3-RRS spherical parallel mechanism," *Adv. Mech. Eng.*, vol. 9, no. 8, Aug. 2017, Art. no. 168781401771811.

[28] D. Eberly. *Euler Angle Formulas*. Accessed: Feb. 16, 2023. [Online]. Available: https://www.geometrictools.com/

[29] E. Emmanouil, G. Wei, and J. S. Dai, "Spherical trigonometry constrained kinematics for a dexterous robotic hand with an articulated palm," *Robotica*, vol. 34, no. 12, pp. 2788–2805, Dec. 2016.

[30] T. Essomba, M. A. Laribi, S. Zeghloul, and G. Poisson, "Optimal synthesis of a spherical parallel mechanism for medical application," *Robotica*, vol. 34, no. 3, pp. 671–686, Mar. 2016.

[31] T. Essomba, J. Sandoval, M. A. Laribi, C.-T. Wu, C. Breque, S. Zeghloul, and J.-P. Richer, "Torque reduction of a reconfigurable spherical parallel mechanism based on craniotomy experimental data," *Appl. Sci.*, vol. 11, no. 14, p. 6534, Jul. 2021.

[32] H. Eves, *Great Moments in Mathematics (Before 1650)* (Dolciani Mathematical Expositions). Washington, DC, USA: Mathematical Association of America, 1983.

[33] D. Feller, "Dexterity, workspace and performance analysis of the conceptual design of a novel three-legged, redundant, lightweight, compliant, serial–parallel robot," *J. Intell. Robotic Syst.*, vol. 109, no. 1, Aug. 2023.

[34] D. Feller and C. Siemers, "Topological analysis of a novel compact omnidirectional three-legged robot with parallel hip structures regarding locomotion capability and load distribution," *Robotics*, vol. 10, no. 4, p. 117, Oct. 2021.

[35] D. Feller and C. Siemers, "Mechanical design and analysis of a novel three-legged, compact, lightweight, omnidirectional, serial–parallel robot with compliant agile legs," *Robotics*, vol. 11, no. 2, p. 39, Mar. 2022.

[36] J.-S. Gao, Y.-C. Wang, D.-P. Liu, and W.-L. Zuo, "Simulation and experiment on the serial–parallel leg of a novel quadruped walking robot," in *Proc. IEEE Int. Conf. Mechatronics Autom.*, Aug. 2016, pp. 165–170.

[37] H. Geyer and U. Saranli, "Gait based on the spring-loaded inverted pendulum," in *Humanoid Robotics: A Reference*, A. Goswami and P. Vadakkepat, Eds. Dordrecht, The Netherlands: Springer, 2018, pp. 1–25, doi: 10.1007/978-94-007-7194-9_43-1.

[38] C. Gosselin and J. Angeles, "The optimum kinematic design of a spherical three-degree-of-freedom parallel manipulator," *J. Mech., Transmissions, Autom. Design*, vol. 111, no. 2, pp. 202–207, Jun. 1989.

[39] C. Gosselin and J. Angeles, "A global performance index for the kinematic optimization of robotic manipulators," *J. Mech. Design*, vol. 113, no. 3, pp. 220–226, Sep. 1991.

[40] C. M. Gosselin and M. Gagné, "A closed-form solution for the direct kinematics of a special class of spherical three-degree-of-freedom parallel manipulators," in *Computational Kinematics '95*, J.-P. Merlet and B. Ravani, Eds. Dordrecht, The Netherlands: Springer, 1995, pp. 231–240.

[41] C. M. Gosselin, J. Sefrioui, and M. J. Richard, "On the direct kinematics of spherical three-degree-of-freedom parallel manipulators of general architecture," *J. Mech. Design*, vol. 116, no. 2, pp. 594–598, Jun. 1994.

[42] C. M. Gosselin, E. S. Pierre, and M. Gagne, "On the development of the Agile eye," *IEEE Robot. Autom. Mag.*, vol. 3, no. 4, pp. 29–37, Dec. 1996.

[43] C. M. Gosselin, "Simulation and computer-aided kinematic design of three-degree-of-freedom spherical parallel manipulators," *J. Robotic Syst.*, vol. 12, no. 12, pp. 857–869, Dec. 1995.

[44] C. M. Gosselin and E. Lavoie, "On the kinematic design of spherical three-degree-of-freedom parallel manipulators," *Int. J. Robot. Res.*, vol. 12, no. 4, pp. 394–402, 1993.

[45] C. M. Gosselin and É. St-Pierre, "Development and experimentation of a fast 3-DOF camera-orienting device," *Int. J. Robot. Res.*, vol. 16, no. 5, pp. 619–630, Oct. 1997.

[46] C. M. Gosselin and J.-F. Hamel, "The Agile eye: A high-performance three-degree-of-freedom camera-orienting device," in *Proc. IEEE Int. Conf. Robot. Autom.*, vol. 1, Dec. 1994, pp. 781–786.

[47] Maxon Group. *Maxon Motor*. Accessed: Mar. 10, 2021. [Online]. Available: https://www.maxongroup.de/

[48] J. Hofschulte, M. Seebode, and W. Gerth, "Parallel manipulator hip joint for a bipedal robot," in *Climbing and Walking Robots*. Berlin, Germany: Springer, 2005, pp. 601–609.

[49] J. Hofschulte, *Zweibeiniger Roboter mit parallelkinematischen Hüftgelenken*. Norderstedt, Germany: Books on Demand GmbH, 2006.

[50] H. Saafi, M. A. Laribi, and S. Zeghloul, "Forward kinematic model resolution of a special spherical parallel manipulator: Comparison and real-time validation," *Robotics*, vol. 9, no. 3, p. 62, Aug. 2020.

[51] Z. Huang and Y. L. Yao, "A new closed-form kinematics of the generalized 3-DOF spherical parallel manipulator," *Robotica*, vol. 17, no. 5, pp. 475–485, Sep. 1999.

[52] The MathWorks. *MATLAB/Simulink (Documentation)*. Accessed: Aug. 1, 2021. [Online]. Available: https://www.mathworks.com/

[53] C. Innocenti and V. Parenti-Castelli, "Echelon form solution of direct kinematics for the general fully-parallel spherical wrist," *Mechanism Mach. Theory*, vol. 28, no. 4, pp. 553–561, Jul. 1993.

[54] P. Ji and H. Wu, "Algebraic solution to forward kinematics of a 3-DOF spherical parallel manipulator," *J. Robotic Syst.*, vol. 18, no. 5, pp. 251–257, 2001.

[55] G. Jian-She, L. Ming-Xiang, L. Yu-Yin, and W. Bao-Tang, "Singularity analysis and dimensional optimization on a novel serial–parallel leg mechanism," *Proc. Eng.*, vol. 174, pp. 45–52, Nov. 2017.

[56] X. Kong and C. M. Gosselin, "A formula that produces a unique solution to the forward displacement analysis of a quadratic spherical parallel manipulator: The Agile eye," *J. Mech. Robot.*, vol. 2, no. 4, Nov. 2010, Art. no. 044501.

[57] J.-A. Leal-Naranjo, M. Wang, J.-C. Paredes-Rojas, and H. Rostro-Gonzalez, "Design and kinematic analysis of a new 3-DOF spherical parallel manipulator for a prosthetic wrist," *J. Brazilian Soc. Mech. Sci. Eng.*, vol. 42, no. 1, p. 63, Jan. 2020.

[58] J. Lee, H. Kim, and W. Yang, "Development of wrist interface based on fully actuated coaxial spherical parallel mechanism for force interaction," *Sensors*, vol. 21, no. 23, p. 8073, Dec. 2021.

[59] G. Legnani and I. Fassi, "Kinematics analysis of a class of spherical PKMs by projective angles," *Robotics*, vol. 7, no. 4, p. 59, Sep. 2018.

[60] K. Li, C. Chen, X. Yuan, Y. He, K. Tao, and W. Gao, "Predictive control of stable standing of three-legged robot," in *Proc. Chin. Autom. Congr. (CAC)*, Nov. 2019, pp. 2797–2802.

[61] O. Mahdizadeh, A. Z. Meymand, M. Mollahossein, and S. A. A. Moosavian, "Kinematics and dynamics modeling of spherical parallel manipulator," in *Proc. 6th RSI Int. Conf. Robot. Mechatronics (IcRoM)*, Oct. 2018, pp. 406–412.

[62] Y. Masuda and M. Ishikawa, "Simplified triped robot for analysis of three-dimensional gait generation," *J. Robot. Mechatronics*, vol. 29, no. 3, pp. 528–535, Jun. 2017.

[63] J. M. McCarthy and G. S. Soh, *Geometric Design of Linkages* (Interdisciplinary Applied Mathematics), 2nd ed. New York, NY, USA: Springer, Dec. 2012, p. XXVIII and 448, doi: 10.1007/978-1-4419-7892-9.

[64] J. P. Merlet, *Parallel Robots* (Solid Mechanics and Its Applications). Amsterdam, The Netherlands: Springer, 2005.

[65] A. Molaei, E. Abedloo, H. D. Taghirad, and Z. Marvi, "Kinematic and workspace analysis of DIAMOND: An innovative eye surgery robot," in *Proc. 23rd Iranian Conf. Electr. Eng.*, May 2015, pp. 882–887.

[66] K. Oki, M. Ishikawa, Y. Li, N. Yasutani, and K. Osuka, "Tripedal walking robot with fixed coxa driven by radially stretchable legs," in *Proc. IEEE/RSJ Int. Conf. Intell. Robots Syst. (IROS)*, Sep. 2015, pp. 5162–5167.

[67] V. Parlaktas, E. Tanik, and Ç. M. Tanik, "On the design of a novel fully compliant spherical four-bar mechanism," *Adv. Mech. Eng.*, vol. 11, no. 9, 2019, Art. no. 1687814019879548.

[68] P. Ren and D. Hong, "Triple stance phase displacement analysis with redundant and nonredundant sensing in a novel three-legged mobile robot using parallel kinematics," *J. Mech. Robot.*, vol. 1, no. 4, Nov. 2009, Art. no. 041001.

[69] RLS. *RLS: Rotary and Linear Motion Sensors*. Accessed: Mar. 10, 2021. [Online]. Available: https://www.rls.si/

[70] A. Rosyid, C. Stefanini, and B. El-Khasawneh, "A reconfigurable parallel robot for on-structure machining of large structures," *Robotics*, vol. 11, no. 5, p. 110, Oct. 2022.
[71] H. Saafi, M. A. Laribi, and S. Zeghloul, "Resolution of spherical parallel manipulator (SPM) forward kinematic model (FKM) near the singularity," in *Proc. 21st Congrés Français de Mécanique*, 2013, pp. 1–6.
[72] H. Saafi, M. A. Laribi, and S. Zeghloul, "Forward kinematic model improvement of a spherical parallel manipulator using an extra sensor," *Mechanism Mach. Theory*, vol. 91, pp. 102–119, Sep. 2015.
[73] H. Saafi, M. Vulliez, S. Zeghloul, and M. A. Laribi, "A new serial approach of the forward kinematic model of spherical parallel manipulators for real-time applications," *Proc. Inst. Mech. Engineers, C, J. Mech. Eng. Sci.*, vol. 232, no. 4, pp. 677–684, Feb. 2018.
[74] S. Sadeqi, S. P. Bourgeois, E. J. Park, and S. Arzanpour, "Design and performance analysis of a 3-RRR spherical parallel manipulator for hip exoskeleton applications," *J. Rehabil. Assistive Technol. Eng.*, vol. 4, Jan. 2017, Art. no. 205566831769759.
[75] N. Saiki, K. Tadakuma, M. Watanabe, K. Abe, M. Konyo, and S. Tadokoro, "Experimental study of the mechanical properties of a spherical parallel link mechanism with arc prismatic pairs," *IEEE Robot. Autom. Lett.*, vol. 7, no. 4, pp. 11221–11227, Oct. 2022.
[76] N. Saiki, K. Tadakuma, M. Watanabe, E. Takane, M. Nobutoki, S. Suzuki, M. Konyo, and S. Tadokoro, "2-DOF spherical parallel mechanism capable of biaxial swing motion with active arc sliders," *IEEE Robot. Autom. Lett.*, vol. 6, no. 3, pp. 4680–4687, Jul. 2021.
[77] A. Seyfarth, H. Geyer, M. Günther, and R. Blickhan, "A movement criterion for running," *J. Biomechanics*, vol. 35, no. 5, pp. 649–655, May 2002.
[78] A. Shintemirov, A. Niyetkaliyev, and M. Rubagotti, "Numerical optimal control of a spherical parallel manipulator based on unique kinematic solutions," *IEEE/ASME Trans. Mechatronics*, vol. 21, no. 1, pp. 98–109, Feb. 2016.
[79] M. Sin, J. H. Cho, H. Lee, K. Kim, H. S. Woo, and J.-M. Park, "Development of a real-time 6-DOF motion-tracking system for robotic computer-assisted implant surgery," *Sensors*, vol. 23, no. 5, p. 2450, Feb. 2023.
[80] I. Tursynbek, A. Niyetkaliye, and A. Shintemirov, "Computation of unique kinematic solutions of a spherical parallel manipulator with coaxial input shafts," in *Proc. IEEE 15th Int. Conf. Autom. Sci. Eng. (CASE)*, Aug. 2019, pp. 1524–1531.
[81] I. Tursynbek and A. Shintemirov, "Infinite rotational motion generation and analysis of a spherical parallel manipulator with coaxial input axes," *Mechatronics*, vol. 78, Oct. 2021, Art. no. 102625.
[82] G. Wu, S. Bai, and J. Kepler, "Mobile platform center shift in spherical parallel manipulators with flexible limbs," *Mechanism Mach. Theory*, vol. 75, pp. 12–26, May 2014.
[83] J. Zhang, C. Liu, T. Liu, K. Qi, J. Niu, and S. Guo, "Module combination based configuration synthesis and kinematic analysis of generalized spherical parallel mechanism for ankle rehabilitation," *Mechanism Mach. Theory*, vol. 166, Dec. 2021, Art. no. 104436.
[84] Z. Zhou and C. Gosselin, "Analysis and design of a novel compact three-degree-of-freedom parallel robot," *J. Mech. Robot.*, vol. 15, no. 5, Oct. 2023, Art. no. 051009.
[85] Y. Zou, A. Zhang, Q. Zhang, B. Zhang, X. Wu, and T. Qin, "Design and experimental research of 3-RRS parallel ankle rehabilitation robot," *Micromachines*, vol. 13, no. 6, p. 950, Jun. 2022.

DAVID FELLER received the B.S. degree in mechanical engineering and the M.S. degree in mechatronics from the Clausthal University of Technology, Clausthal-Zellerfeld, Germany, in 2013 and 2016, respectively. He is currently pursuing the Ph.D. degree in mechanical engineering. Since 2016, he has been a Research Assistant with the Department of Automation Technology, Institute of Electrical Information Technology, Clausthal University of Technology. His research interest includes the ongoing research in the field of legged robots, with a particular focus on mechanism, manipulator, and controller design in robotics.